

Robust characteristics method for modelling multiphase visco-elasto-plastic thermo-mechanical problems

Taras V. Gerya^{a,*}, David A. Yuen^b

^a *Geophysical Fluid Dynamics Group, Institute of Geophysics, Department of Geosciences, Swiss Federal Institute of Technology (ETH-Zurich), CH-8093 Zurich, Switzerland*

^b *Department of Geology and Geophysics and Minnesota Supercomputing Institute, University of Minnesota, Minneapolis, MN 55455, USA*

Received 24 January 2007; received in revised form 26 April 2007; accepted 26 April 2007

Abstract

We have extended our previous 2D method [Gerya, T.V., Yuen, D.A., 2003. Characteristics-based marker-in-cell method with conservative finite-differences schemes for modeling geological flows with strongly variable transport properties. *Phys. Earth Planet. Interiors* 140, 295–320], which is a combination of conservative finite-differences with marker-in-cell techniques to include the effects of visco-elasto-plastic rheology, self-gravitation and a self-consistently derived evolving curvilinear planetary surface. This code is called I2ELVIS and can solve a new class of computationally challenging problems in geodynamics, such as shear localization with large strains, crustal intrusion emplacement of magmas, bending of realistic visco-elasto-plastic plates and core-formation by vigorous shell tectonics activities related to a global Rayleigh–Taylor instability of a metal layer formed around silicate-rich lower density (primordial) core during planetary accretion. We discuss in detail the computational strategy required the rheological constraints to be satisfied at each time step and spatial location. We show analytical benchmarks and examples drawn from comparing between numerical and analogue experiments in structural geology, subducting slab bending with a visco-elasto-plastic rheology and equilibrium spherical configurations from self-gravitation. We have also tested possibilities of future applications by addressing 3D geometries based on multigrid method and including inertial effects in the momentum equation with tracers in order to simulate meteoritic impact events and eventually earthquake instabilities.

© 2007 Elsevier B.V. All rights reserved.

Keywords: Numerical algorithm; Visco-elasto-plasticity; Self-gravitation; Free curvilinear surface; Inertial effects

1. Introduction

Numerical modelling of geodynamics is now recognized as a truly challenging problem in computational science because of the complex non-linear nature of crustal and mantle rheologies and their coupling to multi-component systems and other thermodynamic variables.

In the past we (Gerya and Yuen, 2003) have studied viscous flows with variable viscosity and other variable properties such as thermal conductivity, with a mixed Lagrangian–Eulerian numerical scheme based on conservative finite-differences and marker-in-cell techniques. In this present work we will extend our previously designed methodology to modelling plate processes involving a more realistic rheology which takes into account visco-elasto-plasticity. This new endeavour will open up many new vistas in geological phenomena. We need to consider geodynamical

* Corresponding author. Tel.: +41 44 6336623; fax: +41 44 6331065.
E-mail address: taras.gerya@erdw.ethz.ch (T.V. Gerya).

situations involving large deformation simultaneously together with thermo-mechanical coupling. We will extend our methodology for advection schemes originally designed for scalars to tensor fields (Schmalholz et al., 2001; Moresi et al., 2003; Muhlhaus and Regenauer-Lieb, 2005), which is crucial in visco-elasticity and plasticity. In this paper we do not want to solve any peculiar geophysical problems but rather demonstrate the ability of our method to maintain a grip on challenging geodynamical situations involving strong contrast of rheological properties, large deformation and the consequent multi-scale phenomena. We will also describe a novel method of using a Cartesian code to calculate the non-linear dynamics of a deforming self-gravitating spherical body. This would be extremely important for modelling planetary dynamics.

In Section 2 we will write down the constitutive equations for the visco-elasto-plastic rheology and the accompanying thermo-mechanical equations. We will also lay out the mathematical formulation of the deformation involving a spherical model, using a Cartesian code. In Section 3 we give some analytical benchmarks and illustrative examples of visco-elasto-plastic deformation and shear localization along with results from the coupling of the thermo-mechanics to self-gravitation. Finally, we summarize the novel features of the new code and give some future perspectives, such as addressing issues of 3D geometries and including inertial effects in the momentum equation.

2. Basic background of the scheme for numerical modelling

2.1. Rheological constitutive equations

In the present study we employed a visco-elasto-plastic rheology (e.g., Ranalli, 1995) with the deviatoric strain rate $\dot{\epsilon}_{ij}$ including the three respective components:

$$\dot{\epsilon}_{ij} = \dot{\epsilon}_{ij(\text{viscous})} + \dot{\epsilon}_{ij(\text{elastic})} + \dot{\epsilon}_{ij(\text{plastic})}, \quad (1)$$

where

$$\dot{\epsilon}_{ij(\text{viscous})} = \frac{1}{2\eta} \sigma_{ij}, \quad (1a)$$

$$\dot{\epsilon}_{ij(\text{elastic})} = \frac{1}{2\mu} \frac{D\sigma_{ij}}{Dt}, \quad (1b)$$

$$\dot{\epsilon}_{ij(\text{plastic})} = 0 \quad \text{for } \sigma_{\text{II}} < \sigma_{\text{yield}},$$

$$\dot{\epsilon}_{ij(\text{plastic})} = \chi \frac{\partial G}{\partial \sigma_{ij}} = \chi \frac{\sigma_{ij}}{2\sigma_{\text{II}}} \quad \text{for } \sigma_{\text{II}} = \sigma_{\text{yield}}, \quad (1c)$$

$$G = \sigma_{\text{II}}, \quad (1d)$$

$$\sigma_{\text{II}} = \left(\frac{1}{2}\sigma_{ij}\sigma_{ij}\right)^{1/2}, \quad (1e)$$

where $D\sigma_{ij}/Dt$ is objective co-rotational time derivative of the deviatoric stress component σ_{ij} , σ_{yield} is plastic yield strength for given rock, G is plastic potential of yielding material (e.g., Hill, 1950; Vermeer, 1990), σ_{II} is second deviatoric stress invariant and χ is plastic multiplier, which can be determined locally at each time step and satisfies the plastic yielding condition:

$$\sigma_{\text{II}} = \sigma_{\text{yield}}. \quad (2)$$

Our plastic flow rule formulation (Eq. (1c)) includes deviatoric stress and strain rate components only and consequently our plastic potential formulation (Eq. (1d)) is the same for both dilatant and non-dilatant materials. In the case of plastic deformation of dilatant materials this formulation is, therefore combined with the equation describing volumetric changes computed in 2D in the form of

$$-\frac{D \ln \rho}{Dt} = \text{div}(\bar{v}) = 2 \sin(\psi) \dot{\epsilon}_{\text{II}(\text{plastic})},$$

$$\dot{\epsilon}_{\text{II}(\text{plastic})} = \left(\frac{1}{2}\dot{\epsilon}_{ij(\text{plastic})}\dot{\epsilon}_{ij(\text{plastic})}\right)^{1/2} \quad (3)$$

where ψ is dilatation angle which generally depends on plastic strain (e.g., Hill, 1950) and $\dot{\epsilon}_{\text{II}(\text{plastic})}$ is the second invariant of deviatoric plastic strain rate tensor.

The plastic strength σ_{yield} of a rock generally depends on mean stress on solids ($P_{\text{solid}} = P$) and on pore fluid pressure (P_{fluid}) such that (Ranalli, 1995):

$$\sigma_{\text{yield}} = C + \sin(\varphi)P, \quad (4)$$

$$\sin(\varphi) = \sin(\varphi_{\text{dry}})\lambda, \quad \lambda = \frac{P_{\text{fluid}}}{P_{\text{solid}}}, \quad (5)$$

where C is the cohesion (residual strength at $P=0$), φ is effective internal friction angle (φ_{dry} stands for dry rocks) and λ is the pore fluid pressure factor. For dry fractured crystalline rocks $\sin(\varphi)$ is independent of composition and vary from 0.85 at $P < 200$ MPa to 0.60 at higher pressure (Brace and Kohlstedt, 1980). The plastic strength of dry rocks would strongly increase with pressure to a limit of ~ 9 GPa according to the Peierls mechanism for low temperatures (Kameyama et al., 1999).

The effective viscosity of solid rocks essentially depends on the stress, pressure and temperature. It is defined in terms of the second deviatoric stress invariant (Ranalli, 1995) as

$$\eta = \left(\frac{2}{\sigma_{\text{II}}}\right)^{(n-1)} \frac{F^n}{A_D} \exp\left(\frac{E + PV}{RT}\right), \quad (6)$$

where A_D , E , V and n are experimentally determined flow law parameters (A_D is the pre-exponential factor, E and V are the activation energy and volume) and R is the gas constant. F is a dimensionless coefficient depending on the type of experiments on which the flow law is based (Ranalli, 1995). For example:

$$F = \begin{cases} \frac{2^{(1-n)/n}}{3^{(1+n)/2n}} & \text{for triaxial compression and} \\ 2^{(1-2n)/n} & \text{for simple shear.} \end{cases}$$

2.2. Conservation equations and numerical implementation

We have considered 2D creeping flow wherein both thermal and chemical buoyant forces are included, along with mechanical heating from adiabatic compression and viscous dissipation in the heat conservation equation.

We have adopted a Lagrangian frame (Gerya and Yuen, 2003) in which the heat conservation equation with a variable thermal conductivity $k(T, P, c)$ depending on rock composition (c), pressure and temperature takes the form:

$$\begin{aligned} \rho C_p \left(\frac{DT}{Dt} \right) &= -\frac{\partial q_x}{\partial x} - \frac{\partial q_z}{\partial z} + H_r + H_a + H_s + H_L, \\ q_x &= -k(T, P, c) \frac{\partial T}{\partial x}, \quad q_z = -k(T, P, c) \frac{\partial T}{\partial z}, \\ H_a &= T\alpha \left(v_x \frac{\partial P}{\partial x} + v_z \frac{\partial P}{\partial z} \right), \\ H_s &= \sigma_{xx}(\dot{\epsilon}_{xx} - \dot{\epsilon}_{xx}(\text{elastic})) + \sigma_{zz}(\dot{\epsilon}_{zz} - \dot{\epsilon}_{zz}(\text{elastic})) \\ &\quad + 2\sigma_{xz}(\dot{\epsilon}_{xz} - \dot{\epsilon}_{xz}(\text{elastic})), \end{aligned} \quad (7)$$

where D/Dt represents the substantive time derivative, H_r , H_a , H_s and H_L are the radioactive, adiabatic, shear and latent heating, respectively; other notations are given in Table 1.

The conservation of mass is approximated by the compressible time-dependent 2D continuity equation:

$$\frac{D \ln \rho}{Dt} + \frac{\partial v_x}{\partial x} + \frac{\partial v_z}{\partial z} = 0. \quad (8)$$

The 2D Stokes equations for creeping flow with position and time-dependent gravitational acceleration vector $\bar{g}(x, z, t)$ take the form:

$$\begin{aligned} \frac{\partial \sigma_{xx}}{\partial x} + \frac{\partial \sigma_{xz}}{\partial z} - \frac{\partial P}{\partial x} &= -\rho(T, P, c)g_x(x, z, t), \\ g_x(x, z, t) &= -\frac{\partial \Phi}{\partial x}, \end{aligned} \quad (9)$$

Table 1
Abbreviations and units

Symbol	Meaning
A_D	Material constant ($\text{MPa}^{-n} \text{s}^{-1}$)
C	Cohesion (Pa)
c	Composition
C_p	Isobaric heat capacity ($\text{J kg}^{-1} \text{K}^{-1}$)
E	Activation energy (kJ mol^{-1})
G	Plastic potential (Pa)
g_x, g_z	Horizontal and vertical components of gravitational acceleration (m s^{-2})
H_r, H_a, H_s, H_L	Radioactive, adiabatic, shear and latent heat production (W m^{-3})
k	Thermal conductivity ($\text{W m}^{-1} \text{K}^{-1}$)
n	Stress exponent
P, P_{solid}	Dynamic pressure (mean stress on solids) (Pa)
P_{fluid}	Pore fluid pressure (Pa)
R	Gas constant ($\text{J mol}^{-1} \text{K}^{-1}$)
t	Time (s)
$\Delta t, \Delta t_m, \Delta t_T$	Computational, displacement and thermal time step (s)
T	Temperature (K)
V	Activation volume ($\text{J MPa}^{-1} \text{mol}^{-1}$)
v_x, v_z	Horizontal and vertical components of velocity (m s^{-1})
x, z	Horizontal and vertical coordinates (m)
Z	Visco-elasticity factor
α	Thermal expansion coefficient (K^{-1})
β	Compressibility coefficient (Pa^{-1})
χ	Plastic multiplier (s^{-1})
$\dot{\epsilon}_{II}$	Second invariant of the deviatoric strain rate tensor (s^{-1})
$\dot{\epsilon}_{ij}$	Components of the deviatoric strain rate tensor (s^{-1})
Φ	Gravitational potential (J kg^{-1})
η	Viscosity (Pa s)
η_{vp}	Viscosity-like parameter (Eq. (16)) (Pa s)
φ	Internal friction angle ($^\circ$)
γ	Gravitational constant ($\text{N m}^2 \text{kg}^{-2}$)
λ	Pore fluid pressure coefficient: $\lambda = P_{\text{fluid}}/P_{\text{solid}}$
μ	Shear modulus (Pa)
ρ	Density (kg m^{-3})
σ_{II}	Second invariant of the deviatoric stress tensor (Pa)
σ_{ij}	Components of the deviatoric stress tensor (Pa)
ψ	Dilation angle ($^\circ$)

$$\begin{aligned} \frac{\partial \sigma_{zx}}{\partial x} + \frac{\partial \sigma_{zz}}{\partial z} - \frac{\partial P}{\partial z} &= -\rho(T, P, c)g_z(x, z, t), \\ g_z(x, z, t) &= -\frac{\partial \Phi}{\partial z}, \end{aligned} \quad (10)$$

where $\rho(T, P, c)$ is local density dependent on pressure (P) temperature (T) and composition (c); $g_x(x, y, t)$, and $g_z(x, y, t)$ are components of local gravitational acceleration vector (Fig. 1) and $\Phi(x, z, t)$ is gravitational potential

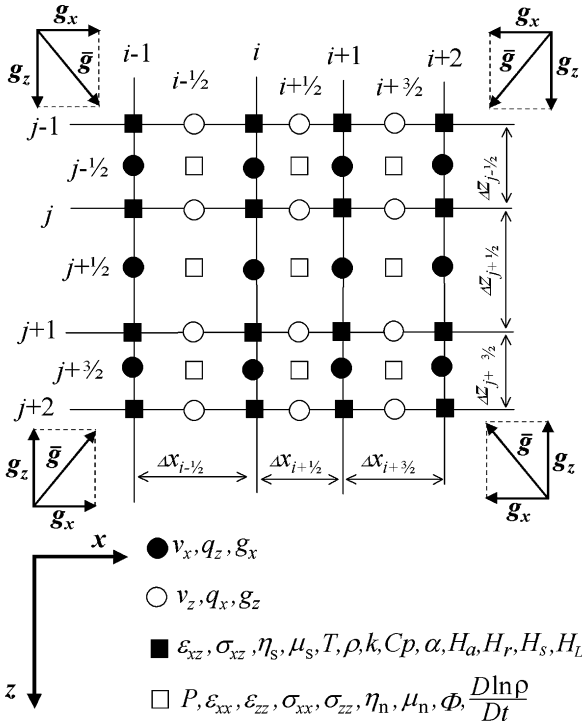


Fig. 1. Schematic representation of non-regular rectangular staggered Eulerian grid used for numerical solution of Eqs. (7)–(11). g_x and g_z are components of position-dependent gravitational acceleration vector which can vary in the x - z coordinate frame. Different symbols correspond to the nodal points for different scalar properties, vectors and tensors. $i, i + 1/2$, etc. and $j, j + 1/2$, etc. indexes represent the staggered grid and denote, respectively, the horizontal and vertical positions of four different types of nodal points. Many variables ($v_x, v_z, g_x, g_z, \sigma_{xx}, \sigma_{xz}, \sigma_{zz}, \dot{\epsilon}_{xx}, \dot{\epsilon}_{xz}, \dot{\epsilon}_{zz}, P, T, \eta, \mu, \rho, k, C_p$, etc.), up to around 25 per one grid cell, are part of the voluminous output in this code. Note that viscosity (η) and shear modulus (μ) are defined in different points when used for computing of normal (σ_{xx}, σ_{zz} , and, respectively, η_n, μ_n) and shear (σ_{xz} , and, respectively, η_s, μ_s) components of deviatoric stress tensor (σ).

computed according to the Poisson equation:

$$\frac{\partial^2 \Phi}{\partial x^2} + \frac{\partial^2 \Phi}{\partial z^2} = 4K\pi\gamma\rho(P, T, c), \quad (11)$$

where γ is gravitational constant and K depends on geometry of self-gravitating body modeled in 2D ($K = 1$ and $2/3$ stand for cylindrical and spherical geometry, respectively). We note that the density is also a time-dependent quantity, because T and c depend on time (t).

The deviatoric stress components σ_{ij} in Eqs. (9) and (10) are formulated from the visco-elasto-plastic constitutive relationships (Eq. (1)) by using an explicit first-order finite-difference scheme in time in order to represent objective time derivatives of visco-elastic

stresses (e.g. Moresi et al., 2003):

$$\frac{D\sigma_{ij}}{Dt} = \frac{\sigma_{ij} - \sigma_{ij}^0}{\Delta t} \quad (12)$$

$$\sigma_{ij} = 2\eta_{vp}\dot{\epsilon}_{ij}Z + \sigma_{ij}^0(1 - Z), \quad (13)$$

$$Z = \frac{\Delta t\mu}{\Delta t\mu + \eta_{vp}}, \quad (14)$$

$$\eta_{vp} = \eta \quad \text{when } \sigma_{II} < \sigma_{yield}, \quad (15)$$

$$\eta_{vp} = \eta \frac{\sigma_{II}}{\eta\chi + \sigma_{II}}, \quad \text{for } \sigma_{II} = \sigma_{yield}, \quad (16)$$

$$\dot{\epsilon}_{xx} = -\dot{\epsilon}_{zz} = \frac{1}{2} \left(\frac{\partial v_x}{\partial x} - \frac{\partial v_z}{\partial z} \right),$$

$$\dot{\epsilon}_{xz} = \dot{\epsilon}_{zx} = \frac{1}{2} \left(\frac{\partial v_x}{\partial z} + \frac{\partial v_z}{\partial x} \right),$$

in which Δt is the computational time step, σ_{ij}^0 is the deviatoric stress tensor from the previous time slice corrected for advection and rotation by using a non-diffusive marker-in-cell technique (e.g. Moresi et al., 2003; Gerya and Yuen, 2003). Z is the visco-elasticity factor (Schmalholz et al., 2001) and η_{vp} is a viscosity-like local Lagrangian parameter computed iteratively at each time step for every marker point to satisfy the plastic yielding condition everywhere ($\eta_{vp} = \eta$ when no plastic yielding occurs) and then interpolated from markers to respective computational grid nodes (cf. open and solid squares in Fig. 1). We note here that the mean stress and not the depth-dependent lithostatic pressure is consistently used in all rheological models by including the yielding condition, which is particularly important for capturing the variations in shear band orientation (e.g. Vermeer, 1990; Poliakov and Herrmann, 1994; Buitert et al., 2006).

2.3. Computational strategy with markers

In order to implement visco-elasto-plastic rheology, compressibility and self-gravitation in our numerical code I2VIS (Gerya and Yuen, 2003), we have modified our conservative finite-difference and marker-in-cell scheme defined over an irregularly spaced staggered grid (Fig. 1) by introducing time dependence of stresses (Eqs. (12)–(14)) and the density (Eqs. (3) and (8)). Schmalholz et al. (2001) and Moresi et al. (2003) also developed a method for calculating visco-elasticity using tracers, but they did not couple it to the energy equation. We show in Fig. 2 a schematic flow-chart for updating at each time step the evolutionary equations contained in Eqs.

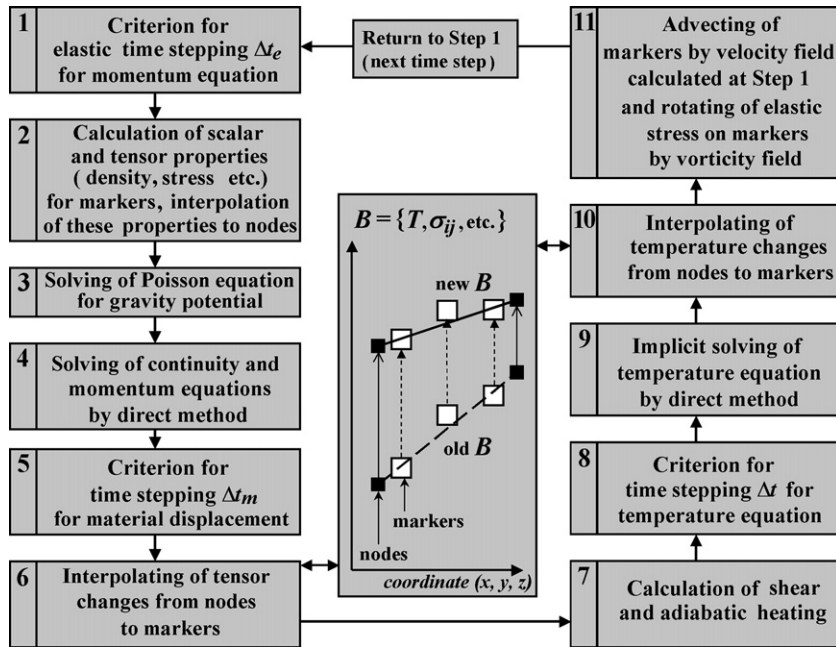


Fig. 2. Flow chart representing the adopted computational strategy used in the programming of the computer code I2ELVIS. Central panel shows the scheme for interpolating the calculated tensor and temperature changes from the Eulerian grid to the moving markers for Steps 6 and 10, respectively. Step 3 can be omitted when prescribed gravitational acceleration field is used in the calculation (cf. Figs. 4–9).

(7)–(11). The steps are as follows (detailed explanation of these steps is given in Sections 2.4–2.7):

1. Defining an optimal computational time step Δt for the momentum and continuity equations. We use a minimum time step value satisfying the following conditions: given absolute time step limit on the order of a minimal characteristic timescale for the processes being modelled; a given relative marker displacement step limit (typically 0.01–1.0 of minimal grid step) corresponding to velocity field calculated at previous time step (see Step 4); a given relative fraction of Lagrangian markers reaching locally yielding condition (Eq. (2)) for the first time (typically 0.0001–0.01 of the total amount of markers with defined plastic yielding condition).
2. Calculating globally the physical properties (η_{vp} , μ , ρ , C_p , k , etc.) for the markers and interpolating these newly calculated properties as well as scalars and tensors defined on markers (T , σ_{ij} , etc.) from the markers to Eulerian nodes (Fig. 1). Plastic yielding condition (Eq. (2)) is controlled locally on markers by using Eq. (13) for predicting the stress changes. This equation is solved in an iterative way for every marker in order to compute η_{vp} and σ_{ij}^0 locally satisfying simultaneously both the viscous (Eq. (6)) and plastic (Eq. (15) and (16)) rheological relationships.
3. Solving Eq. (11) and computing gravitational potential by directly inverting the global matrix with a Gaussian elimination method, which is chosen because of its programming simplicity, stability and high accuracy because of the direct nature of the method. This step is omitted in calculations where prescribed gravitational acceleration field has been used.
4. Solving 2D Eqs. (8)–(10) and computing velocity and pressure by directly inverting the global matrix with a direct Gaussian elimination method.
5. Defining an optimal displacement time step Δt_m for markers (typically limiting maximal displacement to 0.01–1.0 of minimal grid step) which can be generally smaller or equal to the computational time step Δt (see Step 1).
6. Calculating (Eq. (13)) stress changes on the Eulerian nodes for the displacement step Δt_m (see Step 5), interpolating these changes to the markers and calculating new tensor values associated with the markers (see central panel in Fig. 2).
7. Calculating the non-linear shear- and adiabatic heating terms $H_{s(i,j)}$ and $H_{a(i,j)}$ at the Eulerian nodes by using computed velocity, pressure, strain rate and stress fields (see Step 4).
8. Calculating $(DT/Dt)_{(i,j)}$ values at the Eulerian nodes by an explicit scheme and defining an optimal

thermal time step $\Delta t_T \leq \Delta t_m$ (see Step 5) for temperature equation. We use a minimum time step value satisfying the following conditions: given absolute time step limit on the order of a minimal characteristic thermal diffusion timescale for the processes being modeled; given the absolute nodal temperature change limit (typically 1–20 K) corresponding to calculated explicit $(DT/Dt)_{(i,j)}$ values.

9. Solving the non-linear temperature Eq. (7) implicitly in time by a direct Gaussian inversion method.
10. Interpolating calculated nodal temperature changes (see central panel in Fig. 2) from the Eulerian nodes to the markers and calculating new marker temperatures.
11. Using a first-order accurate in space and time explicit Runge–Kutta scheme for advecting all markers throughout the mesh according to the globally calculated velocity field (see Step 4). Components of stress tensor defined on markers are recomputed analytically to account for local stress rotation (e.g. Joseph, 1990; Turcotte and Schubert, 2002). The use of more accurate second-, third- and fourth-order Runge–Kutta advection schemes in case of visco-elasto-plastic flow requires implicit rather than explicit formulation. In this case amount of markers- and nodes-related storage, as well as the CPU time, grow proportionally to the order of the scheme. Returning to Step 1 at the next time step.

We have implemented the above computational algorithm in a new computer code, called I2ELVIS, which is written in the C—computer language. This code has been developed on the basis of our previous viscous thermo-mechanical code (I2VIS) also based on conservative finite-differences and marker-in-cell technique (Gerya and Yuen, 2003). Therefore in the following sections we will concentrate on new modifications and do not give some of the numerical details, which are similar to I2VIS and described extensively in our previous paper (Gerya and Yuen, 2003).

2.4. Interpolation of scalar fields, vectors and tensor fields

According to our algorithmic approach the temperature field and other scalar properties (η , ρ , C_p , C , k , etc.) as well as components of tensors are represented by values ascribed/computed for the multitudinous markers initially distributed on a fine regular marker mesh typically (but not always) with a small ($\leq 1/2$ of marker grid

distance) random displacement (cf. marker distribution in Fig. 4). The effective values of all these parameters at the Eulerian nodal points are interpolated from the markers at each time step. An average number of markers per grid cell commonly vary from $n \times (10^0-10^2)$ depending on the complexity of model configuration (e.g., Brackbill, 1991; Ten et al., 1999; Gerya et al., 2006a; Gorczyk et al., 2007). We always use standard first-order accurate bilinear interpolation schemes between nodes and markers, which are fully described in our previous work (cf. Eqs. (5) and (6) in Gerya and Yuen (2003)).

Our novel modification, however, is the use of more local interpolation schemes for viscosity, shear modulus and deviatoric stress components. In our new staggered grid viscosity (η) and shear modulus (μ) are defined in different points (cf. open and solid squares in Fig. 1) when used for computing of normal (σ_{xx} , σ_{zz} and, respectively, η_n , μ_n) and shear (σ_{xz} , and, respectively η_s , μ_s) components of deviatoric stress tensor. Viscosity, shear modulus and respective stress components for these nodal points are then interpolated from markers found around the nodes at a distance less than half of the local Eulerian grid step. Test calculations show that these new interpolation schemes allow for a better spatial resolution of localization phenomena in case of plastic deformation.

2.5. Finite-difference schemes for discretizing the Poisson equation for the gravitational potential

Discretizing Eq. (11) in 2D is trivial and uses a five-node stencil typical for approximating Poisson equation with finite-differences:

$$\begin{aligned} & \left[\frac{\partial^2 \Phi}{\partial x^2} \right]_{(i+1/2, j+1/2)} + \left[\frac{\partial^2 \Phi}{\partial z^2} \right]_{(i+1/2, j+1/2)} \\ & = 4K\pi\rho_{(i+1/2, j+1/2)}, \\ & \left[\frac{\partial^2 \Phi}{\partial x^2} \right]_{(i+1/2, j+1/2)} \\ & = 2 \frac{\Phi_{(i+3/2, j+1/2)} - \Phi_{(i+1/2, j+1/2)}}{(\Delta x_{(i+1/2)} + \Delta x_{(i+3/2)})\Delta x_{(i+1/2)}} \\ & \quad - 2 \frac{\Phi_{(i+1/2, j+1/2)} - \Phi_{(i-1/2, j+1/2)}}{(\Delta x_{(i-1/2)} + \Delta x_{(i+1/2)})\Delta x_{(i+1/2)}}, \\ & \left[\frac{\partial^2 \Phi}{\partial z^2} \right]_{(i+1/2, j+1/2)} \\ & = 2 \frac{\Phi_{(i+1/2, j+3/2)} - \Phi_{(i+1/2, j+1/2)}}{(\Delta z_{(j+1/2)} + \Delta z_{(j+3/2)})\Delta z_{(j+1/2)}} \end{aligned}$$

$$\begin{aligned}
& -2 \frac{\Phi_{(i+1/2, j+1/2)} - \Phi_{(i+1/2, j-1/2)}}{(\Delta z_{(j-1/2)} + \Delta z_{(j+1/2)}) \Delta z_{(j+1/2)}}, \\
& \rho_{(i+1/2, j+1/2)} \\
& = \frac{1}{4} (\rho_{(i, j)} + \rho_{(i, j+1)} + \rho_{(i+1, j)} + \rho_{(i+1, j+1)}), \quad (17)
\end{aligned}$$

where $i, i + 1/2$ and $j, j + 1/2$ indexes denote, respectively, the horizontal and vertical positions of nodal points corresponding to the different physical parameters (Fig. 1) within the staggered grid. We invert for the global matrix by direct (Gaussian) method for the simultaneous solution of Poisson equation (17) also combined with linear equations describing the boundary conditions for the gravity potential. Gravitational acceleration vector components are then defined in respective Eulerian nodes (see solid and open circles in Fig. 1) by numerical differentiation:

$$[g_x]_{(i, j+1/2)} = -2 \frac{\Phi_{(i+1/2, j+1/2)} - \Phi_{(i-1/2, j+1/2)}}{\Delta x_{(i-1/2)} + \Delta x_{(i+1/2)}}, \quad (18)$$

$$[g_z]_{(i+1/2, j)} = -2 \frac{\Phi_{(i+1/2, j+1/2)} - \Phi_{(i+1/2, j-1/2)}}{\Delta z_{(j-1/2)} + \Delta z_{(j+1/2)}}. \quad (19)$$

The coefficient matrix corresponding to the left part of the discretized equation (17) may remain unchanged throughout the calculation and only right part changes due to the density variations. In this case the decomposition of the coefficient matrix can be done only once, in contrast to other direct solution procedures described in Sections 2.6 and 2.7. However, this matrix may change when staggered grid stepping varies with time following deformation which is an option in our code. The computational time for solving of Eq. (17) is also insignificant compared to that for solving of the momentum and continuity equations. We, therefore, perform a matrix decomposition for Eq. (17) in our code at each time step.

2.6. Finite-difference schemes for discretizing the momentum and continuity equations

The staggered grid shown in Fig. 1 is ideally suitable for the discretization of the momentum and continuity equations. The following FD scheme is a discretized form for representing Eq. (9) to a first-order accuracy in the control volume representation (e.g., Patankar, 1980; Albers, 2000), which allows for the conservation of the visco-elastic stresses between the v_x - and v_z -nodes (see

Fig. 1 for the indexing of the grid points):

$$\begin{aligned}
& \left[\frac{\partial}{\partial x} (2\eta \dot{\epsilon}_{xx} Z) \right]_{(i, j+1/2)} + \left[\frac{\partial}{\partial z} (2\eta \dot{\epsilon}_{xz} Z) \right]_{(i, j+1/2)} \\
& - \left[\frac{\partial P}{\partial x} \right]_{(i, j+1/2)} = - \left[\frac{\partial}{\partial x} (\sigma_{xx}^0 (1 - Z)) \right]_{(i, j+1/2)} \\
& - \left[\frac{\partial}{\partial z} (\sigma_{xz}^0 (1 - Z)) \right]_{(i, j+1/2)} \\
& - \frac{\rho_{(i, j)} + \rho_{(i, j+1)}}{2} [g_x]_{(i, j+1/2)}, \quad (20) \\
& \left[\frac{\partial}{\partial x} (2\eta \dot{\epsilon}_{xx} Z) \right]_{(i, j+1/2)} \\
& = 4 \frac{[\eta \dot{\epsilon}_{xx} Z]_{(i+1/2, j+1/2)} - [\eta \dot{\epsilon}_{xx} Z]_{(i-1/2, j+1/2)}}{\Delta x_{(i-1/2)} + \Delta x_{(i+1/2)}}, \\
& \left[\frac{\partial}{\partial x} (\sigma_{xx}^0 (1 - Z)) \right]_{(i, j+1/2)} \\
& = 2 \frac{[\sigma_{xx}^0 (1 - Z)]_{(i+1/2, j+1/2)} - [\sigma_{xx}^0 (1 - Z)]_{(i-1/2, j+1/2)}}{\Delta x_{(i-1/2)} + \Delta x_{(i+1/2)}}, \\
& \left[\frac{\partial}{\partial z} (2\eta \dot{\epsilon}_{xz} Z) \right]_{(i, j+1/2)} \\
& = 2 \frac{[\eta \dot{\epsilon}_{xz} Z]_{(i, j+1)} - [\eta \dot{\epsilon}_{xz} Z]_{(i, j)}}{\Delta z_{(j+1/2)}}, \\
& \left[\frac{\partial}{\partial z} (\sigma_{xz}^0 (1 - Z)) \right]_{(i, j+1/2)} \\
& = \frac{[\sigma_{xz}^0 (1 - Z)]_{(i, j+1)} - [\sigma_{xz}^0 (1 - Z)]_{(i, j)}}{\Delta z_{(j+1/2)}}, \\
& \left[\frac{\partial P}{\partial x} \right]_{(i, j+1/2)} = 2 \frac{P_{(i+1/2, j+1/2)} - P_{(i-1/2, j+1/2)}}{\Delta x_{(i-1/2)} + \Delta x_{(i+1/2)}}, \\
& [\sigma_{xx}^0 (1 - Z)]_{(i+1/2, j+1/2)} \\
& = \frac{[\eta_n]_{(i+1/2, j+1/2)} [\sigma_{xx}^0]_{(i+1/2, j+1/2)}}{\Delta t [\mu_n]_{(i+1/2, j+1/2)} + [\eta_n]_{(i+1/2, j+1/2)}}, \\
& [\sigma_{xz}^0 (1 - Z)]_{(i, j)} = \frac{[\eta_s]_{(i, j)} [\sigma_{xz}^0]_{(i, j)}}{\Delta t [\mu_s]_{(i, j)} + [\eta_s]_{(i, j)}}, \\
& [\eta \dot{\epsilon}_{xx} Z]_{(i+1/2, j+1/2)}
\end{aligned}$$

$$\begin{aligned}
& \frac{\Delta t[\mu_n]_{(i+1/2, j+1/2)}[\eta_n]_{(i+1/2, j+1/2)}}{\Delta t[\mu_n]_{(i+1/2, j+1/2)} + [\eta_n]_{(i+1/2, j+1/2)}}, \\
[\eta \dot{\epsilon}_{xz} Z]_{(i, j)} &= \frac{\Delta t[\mu_s]_{(i, j)}[\eta_s]_{(i, j)}[\dot{\epsilon}_{xz}]_{(i, j)}}{\Delta t[\mu_s]_{(i, j)} + [\eta_s]_{(i, j)}}, \\
[\dot{\epsilon}_{xx}]_{(i+1/2, j+1/2)} &= \frac{[v_x]_{(i+1, j+1/2)} - [v_x]_{(i, j+1/2)}}{2\Delta x_{(i+1/2)}} \\
&\quad - \frac{[v_z]_{(i+1/2, j+1)} - [v_z]_{(i+1/2, j)}}{2\Delta z_{(j+1/2)}} \\
[\dot{\epsilon}_{xz}]_{(i, j)} &= \frac{[v_x]_{(i, j+1/2)} - [v_x]_{(i, j-1/2)}}{\Delta z_{(j-1/2)} + \Delta z_{(j+1/2)}} \\
&\quad + \frac{[v_z]_{(i+1/2, j)} - [v_z]_{(i-1/2, j)}}{\Delta x_{(i-1/2)} + \Delta x_{(i+1/2)}}
\end{aligned}$$

where σ_{xz}^0 and σ_{xx}^0 are the deviatoric stress tensor components from the previous time step corrected for advection and rotation which are interpolated from markers; Δt is computational time step. Discretization of Eq. (10) is analogous to Eq. (20).

The time-dependent compressible continuity Eq. (8) is discretized as follows:

$$\begin{aligned}
& \frac{[v_x]_{(i+1, j+1/2)} - [v_x]_{(i, j+1/2)}}{\Delta x_{(i+1/2)}} \\
& + \frac{[v_z]_{(i+1/2, j+1)} - [v_z]_{(i+1/2, j)}}{\Delta z_{(j+1/2)}} \\
& = - \left[\frac{D \ln \rho}{Dt} \right]_{(i+1/2, j+1/2)}, \quad (21)
\end{aligned}$$

where $D \ln \rho / Dt$ is density changes (e.g. Eq. (3)) interpolated from markers.

We invert for the global matrix by a highly accurate, direct (Gaussian) method for the simultaneous solution of both the momentum Eq. (20), and the continuity equations Eq. (21) which are also combined with the linear equations describing the boundary conditions for the velocity and pressure. We would like to emphasize once again that we directly solve for the primitive variables (pressure–velocity formulation, e.g. Tackley, 2000; Albers, 2000) rather than for stream-function used in earlier two-dimensional numerical models based on finite-differences (e.g., Weinberg and Schmeling, 1992).

After defining material displacement time step Δt_m the changes in the effective stress field for the Eulerian

nodes are calculated in respective nodal points according to Eq. (13) as

$$\Delta \sigma_{xx} = (2\dot{\epsilon}_{xx}\eta_n - \sigma_{xx}^0) \frac{\mu_n \Delta t_m}{\eta_n + \mu_n \Delta t_m}, \quad (22)$$

$$\Delta \sigma_{xz} = (2\dot{\epsilon}_{xz}\eta_s - \sigma_{xz}^0) \frac{\mu_s \Delta t_m}{\eta_s + \mu_s \Delta t_m}. \quad (23)$$

Correspondent stress increments for markers are then added from the nodes using standard first-order interpolation schemes (cf. Eq. (6) in Gerya and Yuen (2003)) and new updated values of stress components (${}^t\sigma_m$) are, thus obtained for markers.

The interpolation of the calculated stress component changes from the Eulerian nodal points to the moving markers is similar to our temperature interpolation strategy developed before (Gerya and Yuen, 2003) and prevents effectively the problem of numerical diffusion. This feature represents one of the highlights of our computation strategy for solving the time dependent momentum equation using markers. This method does not produce any smoothing of the stress distributions between adjacent markers (cf. central panel in Fig. 2), thus allowing us to resolve the stress structure of a numerical model in much finer details.

However, similar to the advection of temperature field, the main problem with treating advection and rotation of stresses using this incremental update scheme is that all the stirred-structures and instabilities on a subgrid (marker) scale cannot be damped out by grid-scale corrections. For example, in case of strong chaotic mixing of markers, our method may produce numerical oscillations of stress field ascribed to the adjacent markers. These oscillations do not damp out with time on a characteristic Maxwell visco-elastic relaxation timescale. The introduction of a consistent sub-grid numerical stress relaxation operation, which does not change the convergence of the grid scale stress values is a possible solution to this problem. We use here a weak numerical stress relaxation occurring over a characteristic Maxwell time for visco-elastic relaxation. This is implemented by correcting the updated marker stresses (${}^t\sigma_m$) according to the relation:

$$\begin{aligned}
{}^t\sigma_m(D) &= {}^1\sigma_m - [{}^1\sigma_m - {}^t\sigma_m] \exp\left(-\frac{d\Delta t_m}{\Delta t_0}\right), \\
\Delta t_0 &= \frac{\eta_m}{\mu_m} \quad (24)
\end{aligned}$$

where Δt_0 is a characteristic Maxwell timescale of the local visco-elastic relaxation defined for the corresponding marker; ${}^t\sigma_m(D)$ is m th-marker stress corrected for the numerical relaxation; d is dimensionless numerical

relaxation coefficient (we use empirical values in the range of $0 \leq d \leq 1$); ${}^1\sigma_m$, is updated stress interpolated from surrounding nodes for the given marker position; μ_m and η_m are shear modulus and viscosity-like parameter (η_{vp}) for given marker, respectively. As in the case for treating the temperature field, we also introduce compensating corrections (cf. Eqs. (13) and (13a) in Gerya and Yuen, 2003) for the marker stresses to conserve original (i.e. before numerical relaxation) nodal stress values.

Introducing the numerical relaxation + compensation operation removes the unrealistic subgrid oscillations over the characteristic local Maxwell visco-elastic relaxation time scale without affecting the accuracy of numerical solution of the momentum equation. Realistic subgrid oscillations will, however, be preserved by this scheme been related for example to the rapid mixing by advection dominating flows.

2.7. Numerical techniques for solving the temperature equation

Numerical techniques for discretizing and solving temperature equation are exactly the same as in the viscous version of our numerical code (I2VIS) and these techniques are fully described in our previous paper (Gerya and Yuen, 2003). The only new modification is a possibility to have multiple thermal time steps Δt_T per single material displacement time step Δt_m when $\Delta t_T < \Delta t_m$ condition has to be satisfied. Obviously, in this case the sum of the multiple thermal time steps is equal to one material displacement time step. We note that the time steps will be smaller because of the presence of thermo-mechanical coupling with visco-elastic and visco-plastic rheologies (Regenauer-Lieb and Yuen, 2004).

3. Results from specific examples

In this section we will display results taken from carrying out several calibrating tests of the numerical solutions in order to verify the efficacy of our methods for a variety of circumstances relevant to geodynamics and planetary processes. These will include:

- elastic stress build-up and advection (tests 1 and 2);
- localization of visco-elasto-plastic deformation (tests 3 and 4);
- large simultaneous deformation of materials with contrasting rheological properties (test 5);
- deformation of self-gravitating bodies with thermo-mechanical coupling (test 6);

Numerical experiments discussed in Sections 3.1–3.6 show stability and high accuracy of the algorithm at moderate to high resolution for both Eulerian nodes ($n \times (10^4-10^5)$) and markers ($n \times (10^5-10^6)$). These experiments require moderate computation time of several hours (Sections 3.1–3.2) to several days (Sections 3.3–3.6) on an ordinary PC/workstation with a 2.4 GHz clock.

3.1. Stress build-up for visco-elastic Maxwell body

In case of uniform deformation of an initially unstressed, incompressible visco-elastic medium with a constant strain rate $\dot{\epsilon}_{ij}$ elastic deviatoric stress σ_{ij} grows with time according to the equation:

$$\sigma_{ij} = 2\dot{\epsilon}_{ij}\eta(1 - e^{-\mu t/\eta}), \quad (25)$$

where t is time from the beginning of the deformation and η and μ is the constant viscosity and shear modu-

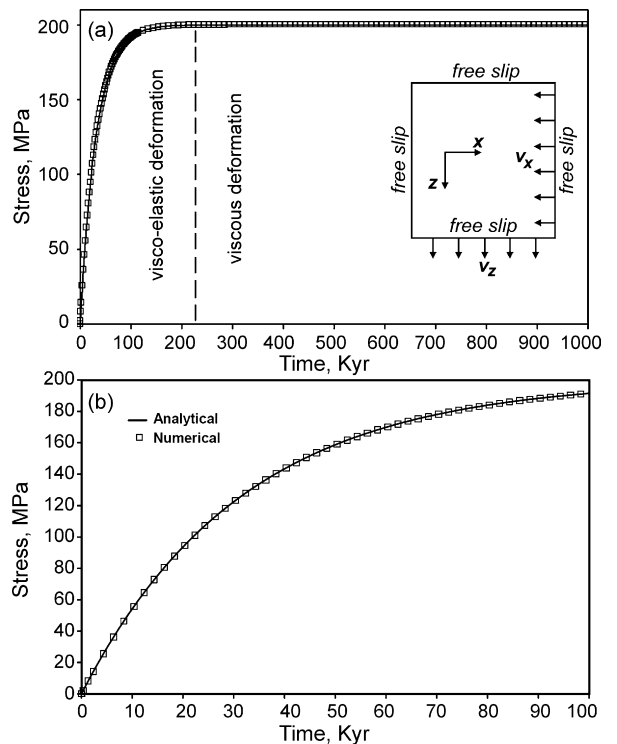


Fig. 3. Numerical solutions for the case of viscoelastic stress build-up due to pure shear (x - z direction) with constant normal strain rate and in the absence of gravity. Numerical and analytical (Eq. (25)) solutions are compared for $\dot{\epsilon}_{zz} = 10^{-14} \text{ s}^{-1}$, $\eta = 10^{22} \text{ Pa s}$ and $\mu = 10^{10} \text{ Pa}$. (a) Numerical results for the complete experiment (strain = 0–0.3). (b) Zoom-in of initial stages of the experiment (strain = 0–0.03). Panel with numerical setup is shown in the right part of the diagram (a). Staggered grid resolution: 101×101 basic nodes (cf. solid rectangles in Fig. 1), 250,000 randomly distributed markers.

lus of the medium, respectively. Based on this equation, we performed numerical test of stress build-up shown in Fig. 3. The numerical experiment was designed on a rectangular model (cf. panel in Fig. 3a) by prescribing time dependent convergence velocity v_x for the right boundary and divergence velocity v_z for the bottom of the model computed as

$$v_x = -\dot{\epsilon}L_x(t), \quad v_z = \dot{\epsilon}L_z(t),$$

where $\dot{\epsilon}$ is prescribed deviatoric strain rate, $L_x(t)$ and $L_z(t)$ are, respectively, horizontal and vertical dimensions of the model at given time t . Model dimensions were changing at each time step Δt as

$$L_x(t + \Delta t) = L_x(t)(1 - \dot{\epsilon}\Delta t),$$

$$L_z(t + \Delta t) = \frac{L_z(t)}{1 - \dot{\epsilon}\Delta t}.$$

Grid spacing was also changing, respectively. At each time step all the deviatoric stress components were inter-

polated from randomly distributed markers to nodes and stress increments were then interpolated back to markers (Fig. 2) after numerically solving the momentum and continuity equations for the entire model domain. Fig. 3 demonstrates the high accuracy of numerical solution, which overlaps with the analytical one properly describing transition from the dominant elastic regime to the prevailing viscous deformation.

3.2. Recovery of the original shape of an elastic slab

Fig. 4 shows results of numerical experiments for the recovery of original shape of the elastic slab surrounded by the weak medium with a much lower viscosity and density. The initially unstressed slab is attached to the bottom of the box and is spontaneously deformed within 2 Kyr under a purely horizontal gravity field ($g_x = 9.81 \text{ m/s}^2$, $g_z = 0$). The slab is deformed

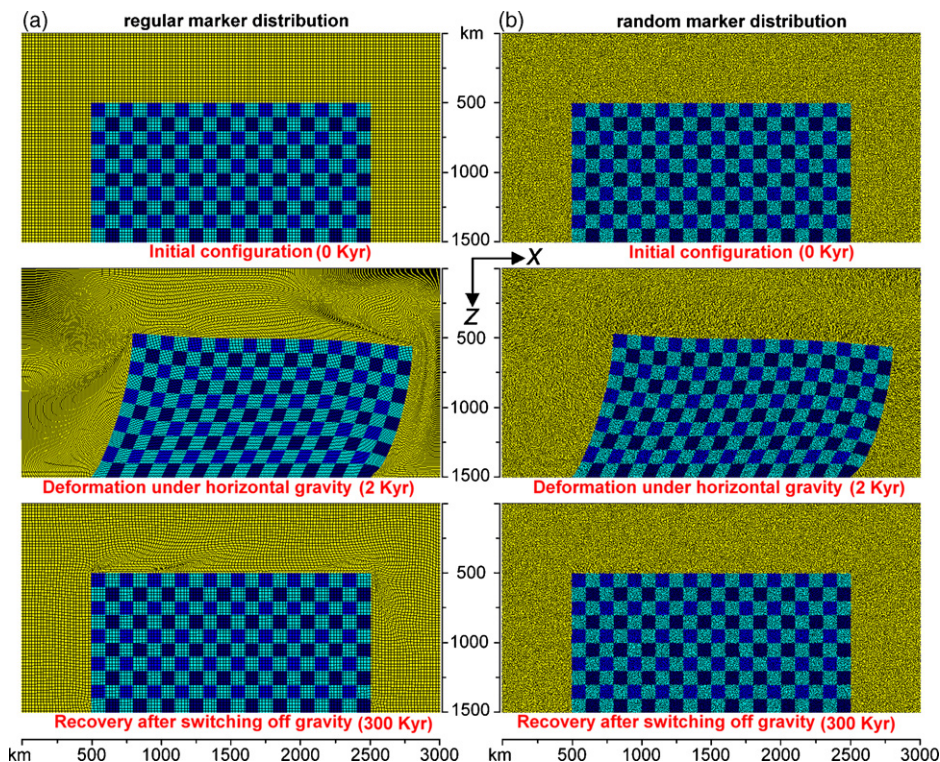


Fig. 4. Results of numerical experiments for the recovery of original shape of the elastic slab (blue, $\rho = 3300 \text{ kg/m}^3$, $\eta = 10^{25} \text{ Pa s}$ and $\mu = 10^{10} \text{ Pa}$) embedded in the weak medium (yellow, $\rho = 1 \text{ kg/m}^3$, $\eta = 10^{19} \text{ Pa s}$ and $\mu = 10^{10} \text{ Pa}$). The slab is attached to the bottom of the box and is initially deformed elastically during 2 Kyr due to the constant horizontal gravity ($g_x = 9.81 \text{ m/s}^2$, $g_z = 0$). The slab fully recover its original shape after switching off gravity (i.e. after $g_x = g_z = 0$ condition is applied at 2 Kyr) since the time of initial elastic deformation (2 Kyr) is much less then the Maxwell time (32,000 Kyr). In contrast, weak medium is subjected to irreversible viscous deformation since its Maxwell time is low (0.032 Kyr). Boundary conditions: no slip at the lower boundary and free slip at all other boundaries. Blue and yellow dots represent positions of markers for the slab and the medium, respectively. Grid resolution of the model is 101×51 nodes, 125,000 markers. (a) Experiment with initially regular distribution of markers. (b) Experiment with initially random distribution of markers. (For interpretation of the references to colour in this figure legend, the reader is referred to the web version of the article.)

almost purely elastically due to the large Maxwell time (32,000 Kyr) of slab material compared to the deformation time (2 Kyr). In contrast, the low viscosity medium is subjected to irreversible viscous deformation since its Maxwell time (0.032 Kyr) is much lower than the deformation time. The degree of elastic deformation is high (Fig. 4, at 2 Kyr) and stresses stored on markers are, therefore, subjected to significant advection and rotation under dominating simple shear deformation. After the no gravity condition ($g_x = g_z = 0$) is applied to the model, the slab fully recover its original shape (Fig. 4, 300 Kyr). Results appear equally good for both regular (Fig. 4a) and random (Fig. 4b) distribution of markers.

3.3. Numerical sandbox benchmark

Numerical modelling of sandbox experiments poses significant computational challenges requiring that numerical code is able to (1) calculate large deformations along spontaneously forming narrow shear zones, (2) represent complex boundary conditions, including frictional boundaries and free surfaces, and (3) include a complex rheology involving both viscous and frictional/plastic materials. These challenges reflect directly the state-of-the-art requirements for numerical modelling of large-scale tectonic processes. We participated in numerical sandbox benchmark conducted by Buitert et al. (2006) for both shortening (Figs. 5 and 6) and exten-

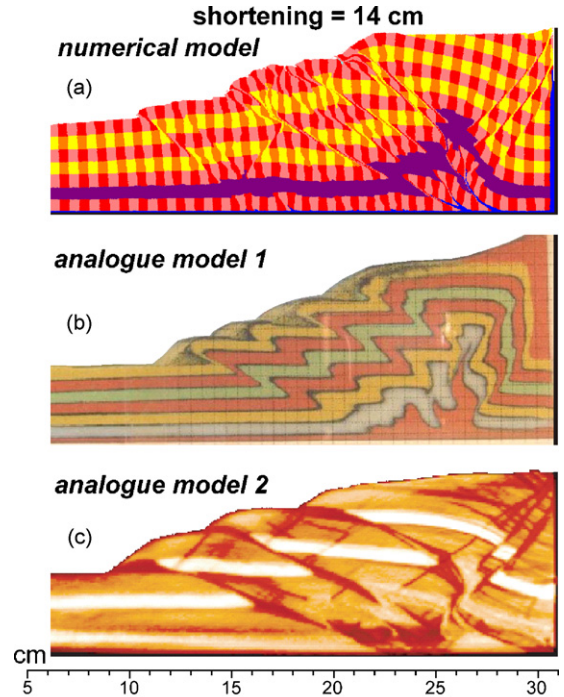


Fig. 6. Comparison of numerical (a) and selected analogues (b), (c) models for the shortening sandbox experiments (Buitert et al., 2006). (a) Code I2ELVIS, Fig. 5; (b) University of Parma; (c) IFP Rueil–Malmaison. See Buitert et al. (2006) for further details of numerical and analogue experiments and material properties.

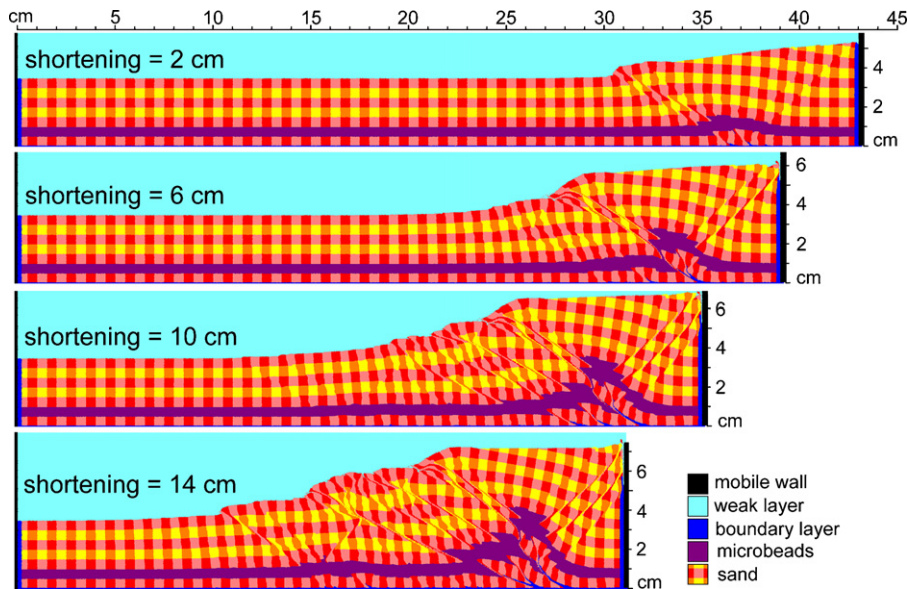


Fig. 5. Results for the shortening numerical sandbox experiment (Buitert et al., 2006). 60×8 cm numerical model with non-uniform numerical grid (944×165 nodes, 2,000,000 randomly distributed markers) employ internal mobile wall (black) moving to the left with constant velocity of 2.5 cm/h. Initial size of deforming part of the model shown here is 45 cm; grid resolution in this part is $0.5 \text{ mm} \times 0.5 \text{ mm}$ (910×165 nodes, 1,500,000 markers). See Buitert et al. (2006) for further details of numerical experiment and material properties.

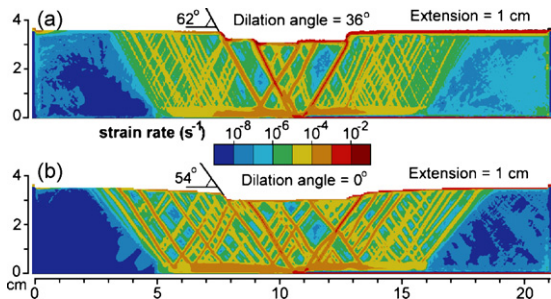


Fig. 7. Results for the extension numerical sandbox experiment (Buiter et al., 2006). 35 cm \times 4.5 cm numerical model with non-uniform numerical grid (539 \times 95 nodes, 650,000 randomly distributed markers) employ internal mobile wall (in the right part of the model) with attached 10 cm wide and 1 mm-thick bottom layer moving to the right with constant velocity of 2.5 cm/h. Initial size of deforming part of the model shown here is 20 cm; grid resolution in this part is 0.5 mm \times 0.5 mm (400 \times 95 nodes, 350,000 markers). (a) Experiment with dilatant sand ($\psi = \varphi = 36^\circ$); (b) experiment with non-dilatant sand ($\psi = 0$, $\varphi = 36^\circ$). Note steeper angle of inclination of shear bands for (a) compared to (b). See Buiter et al. (2006) for further details of numerical experiment and material properties.

sion (Fig. 7) settings. In this benchmark the I2ELVIS code showed the ability to hold up for large deformation, thus demonstrating strong localization of deformation along with spontaneously forming narrow (one to two grid cell wide) shear zones and reproduced structural pattern for both forward and reverse faults (Fig. 5), thus closely matching results of analogue experiments (Fig. 6). The difference between numerical and analogue modelling results occurred on the same order as the differences between analogue models from the different laboratories (cf. Fig. 6a–c). Our plasticity treatment approach allows for modelling both dilatant (Fig. 7a) and non-dilatant (Fig. 7b) materials. The dip angle (α) of shear bands in extensional setting ranges between 45° (Roscoe angle) and $45^\circ + \varphi/2$ (Coulomb angle) (Vermeer, 1990), typically following the relation $\alpha = 45^\circ + (\varphi + \psi)/4$ (Fig. 7). This dip angle is not explicitly “chosen” by the code but forms spontaneously during the propagation of shear bands involving markers for which yielding condition given by Eq. (2) is satisfied locally.

3.4. Visco-elasto-plastic slab bending

Modelling of slab bending is of crucial importance for geodynamics since this process is always associated with subduction and is related to the structural and seismic features at the trench area (e.g. Ranero et al., 2003, 2005). Of special interest is bending-related faulting of the incoming plate creating a pervasive tectonic fabric that cuts across the crust, penetrating deep into the man-

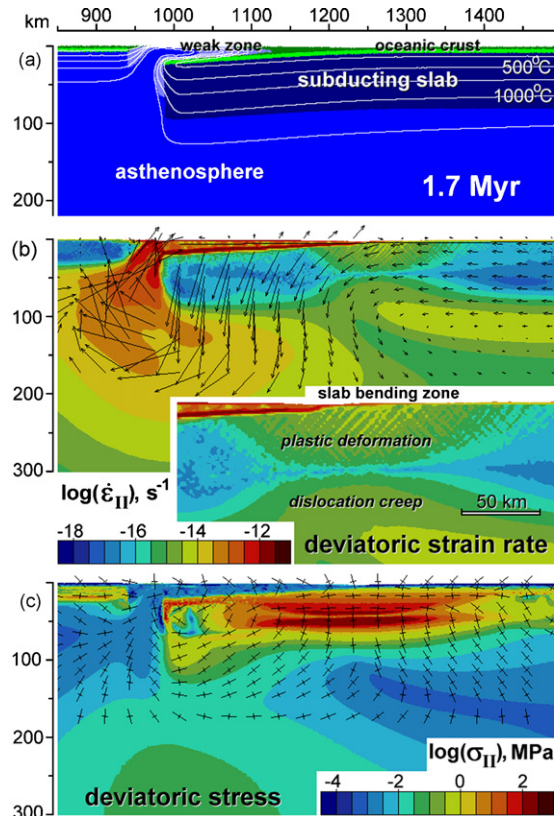


Fig. 8. Results of numerical test for visco-elasto-plastic slab bending during spontaneous initiation of subduction (Gerya et al., 2006b). 640 \times 300 km high-resolution (320 \times 90 nodes, 120,000 markers) area of original 3000 km \times 2500 km model with non-uniform numerical grid (520 \times 164 nodes, 4,570,000 randomly distributed markers) is shown. Two plates of different ages (1 and 70 Myr for the left and right plate, respectively) are juxtaposed together along the transform fault. Initial zone of wet fractured rocks (c.f. light blue zone in (a)) with low plastic strength ($\sin(\varphi) = 0$) was present along the fault that created favorable conditions for spontaneous initiation of subduction (Hall et al., 2003) and slab bending. (a) Distribution of different rock types (color code) and isotherms (white lines); (b) strain rate (color code) and velocity (black arrows) distribution, zoom-in shows slab bending area; (c) deviatoric stress distribution (color code) and stress principal axis orientation (elongated crosses, long and short branches of the crosses show extension and shortening directions, respectively). (For interpretation of the references to colour in this figure legend, the reader is referred to the web version of the article.)

tle (Ranero et al., 2003, 2005). Faulting is active across the entire ocean trench slope, promoting hydration of the cold crust and upper mantle surrounding these deep active faults. The along-strike length and depth of penetration of these faults are also similar to the dimensions of the rupture area of intermediate-depth earthquakes. Fig. 8 shows the results of numerical test for spontaneous bending process of incoming plate during subduction (Gerya et al., 2006b). In the beginning of this experiment

two plates of different ages are juxtaposed together along the transform fault (cf. light blue zone in Fig. 8a) with low plastic strength ($\sin(\varphi)=0$) creating favorable conditions for spontaneous initiation of subduction (Hall et al., 2003) and the concurrent slab bending. Deformation pattern in slab bending area is quite distinct (Fig. 8b): the top of the slab is subjected to intense plastic deformation with localized faults zones while the bottom of the slab is deformed in a ductile way by dislocation creep (cf. Eq. (6)) with enhancement of the deformation (cf. zoom in Fig. 8b) due to high stresses (Fig. 8c) in the bending area. The plastic deformation and dislocation creep fields are, respectively, characterized by extension and compression in a horizontal direction (cf. orientation of stress principal axes in Fig. 8c). These two fields are clearly separated by the narrow non-deforming area in the core of the slab (cf. zoom in Fig. 8b) characterized by low deviatoric stresses (Fig. 8c). The depth of penetration of localized faults (10–50 km) and their preferential dip direction toward the trench (Fig. 8b) are in line with the natural observations (Ranero et al., 2003, 2005). Results of our experiments suggest that in case of free surface condition atop the slab it can be easily bent by its own weight triggering spontaneous retreating subduction. The bending process is facilitated (i) by lowered pressure in the extension region favouring deep penetration of faults and (ii) by high stresses in the compression

region resulting in local lowering of slab viscosity due to the power-law nature of dislocation creep (Eq. (6)).

3.5. Magmatic dike injection into the elasto-plastic crust

Thermo-mechanical modelling of magma intrusion is numerically challenging because it involves simultaneous and intense deformation of materials with very contrasting rheological properties, especially in the formation of dikes. The country crustal rocks are visco-elasto-plastic while the intruding magma is a very low viscosity, complex fluid. Gerya and Burg (2007) have recently employed the code I2ELVIS for modelling of ultramafic magma intrusion process and have found dike intrusion. It has been demonstrated that this code cope well (Fig. 9) with free surface condition and large contrast of rheological properties of involved materials and allows reproducing of basic shapes of intrusive magmatic bodies. It has also been demonstrated that the general shape of the pluton is sensitive to the magma viscosity and the relative elastic, viscous and plastic parts of the crustal rheology. In particular, magmatic dikes (Fig. 9) are formed in case of lowered magma viscosity and elasto-plastic rather than viscous deformation of the crust (Gerya and Burg, 2007).

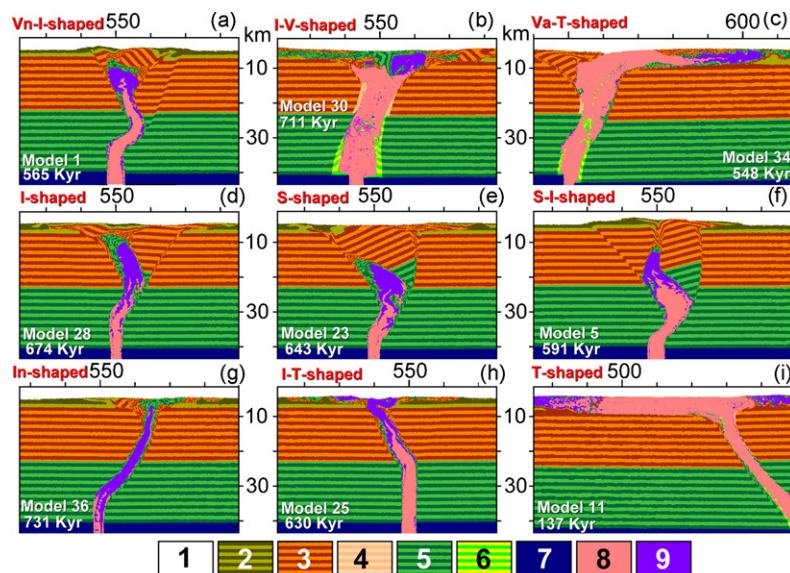


Fig. 9. Major types of culminate shapes of dike-like magmatic bodies obtained in numerical simulations of mafic–ultramafic intrusions emplacement (Gerya and Burg, 2007). Enlarged 65 km × 40 km areas of the original 1100 km × 300 km models are shown. Red letters denote intrusion shapes: V, funnel-shaped; I, finger-shaped; S, sickle-shaped; T, nappe(sill)-shaped; a, asymmetric; n, narrow. Color code: 1 = weak layer (air, water); 2 = sediments; 3 and 4 = upper crust (3, solid; 4, molten); 5 and 6 = lower crust (5, solid; 6, molten); 7 = lithospheric mantle; 8 = crystallized peridotite; 9 = crystallized gabbro. See Gerya and Burg (2007) for further details of numerical experiments and discussion. (For interpretation of the references to colour in this figure legend, the reader is referred to the web version of the article.)

3.6. Deformation of a self-gravitating body

Numerical modelling of deformation of self-gravitating planetary body requires computing of the gravity field which changes with time in response to variations in mass distribution inside the planet. Changes in shape of the planet and related planetary surface deformation should also be considered. In order to tackle these requirements, I2ELVIS uses novel “spherical-Cartesian” approach allowing computing of self-gravitating body of arbitrary form on Cartesian grid and satisfying closely free surface condition:

- (1) The body is surrounded by the weak medium (e.g. Fig. 4) of very low density ($\leq 1 \text{ kg/m}^3$) and low viscosity allowing high (10^1 to 10^6) viscosity contrast at the planetary surface.
- (2) The gravity field is computed (Fig. 10) by solving the Poisson equation for the gravitational poten-

tial (Eq. (11)) associated with the mass (density) distribution portrayed by the tracers at each time step.

- (3) During the solution of the momentum equation, the components of gravitational acceleration vector are computed locally by numerical differentiation of the gravitational potential (Eqs. (18) and (19)) at the corresponding nodal points.

As shown from our test experiments (Figs. 11, 12 and 15), the spontaneously formed planetary surface is numerically stable under conditions of very strong internal deformation inside the planet. Also, spontaneously forming spherical/cylindrical shape of the body is characteristic for stable density distribution (i.e. when density increases toward the core of the body cf. final stages of Figs. 11, 12 and 15). No evidence for non-spherical Cartesian grid dependence of this stable shape was discerned.

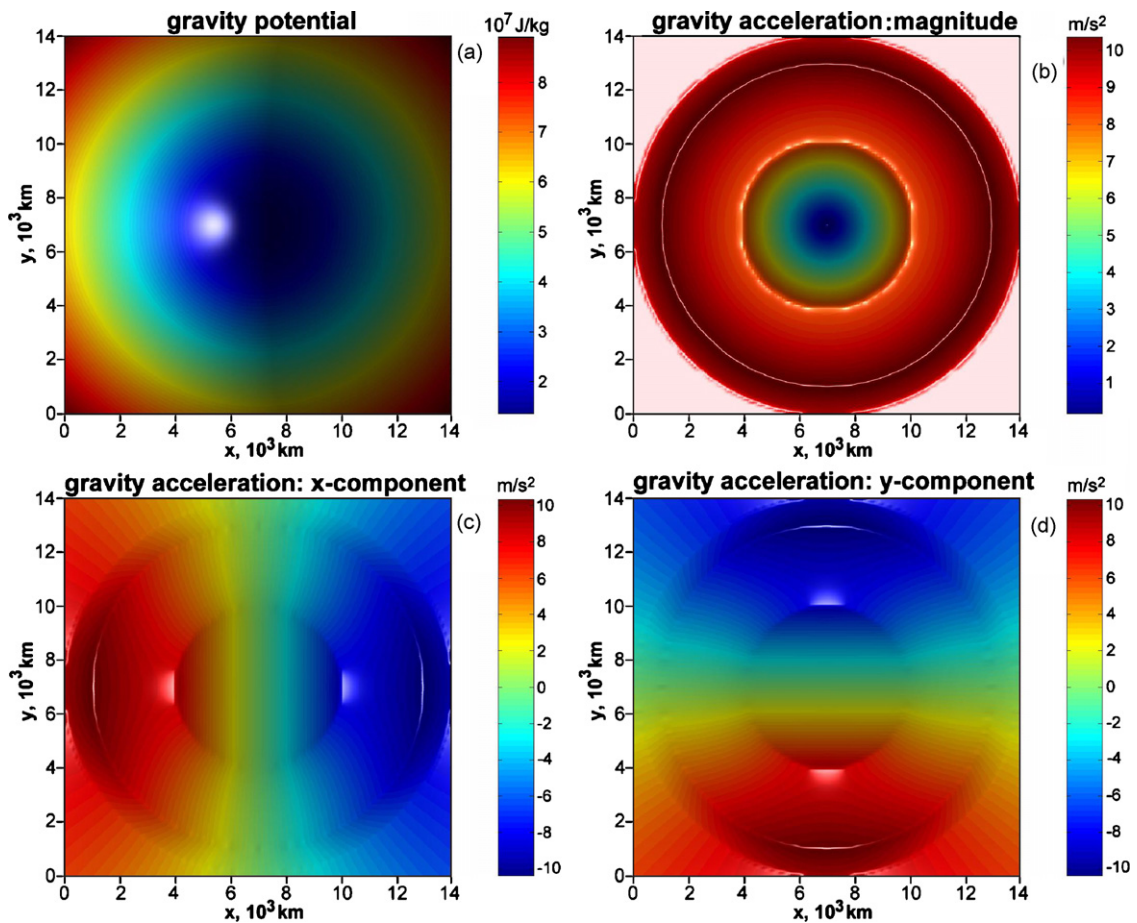


Fig. 10. Numerical solution of the Poisson equation for gravity potential (Eq. (11)) in case of radial two-layered (high-density core + low density mantle) density distribution. (a) Gravity potential, Φ ; (b) gravity vector magnitude, $(g_x^2 + g_y^2)^{1/2}$; (c) and (d) horizontal, g_x , and vertical, g_z , gravity vector components, respectively. Numerical grid resolution is 201×201 nodes.

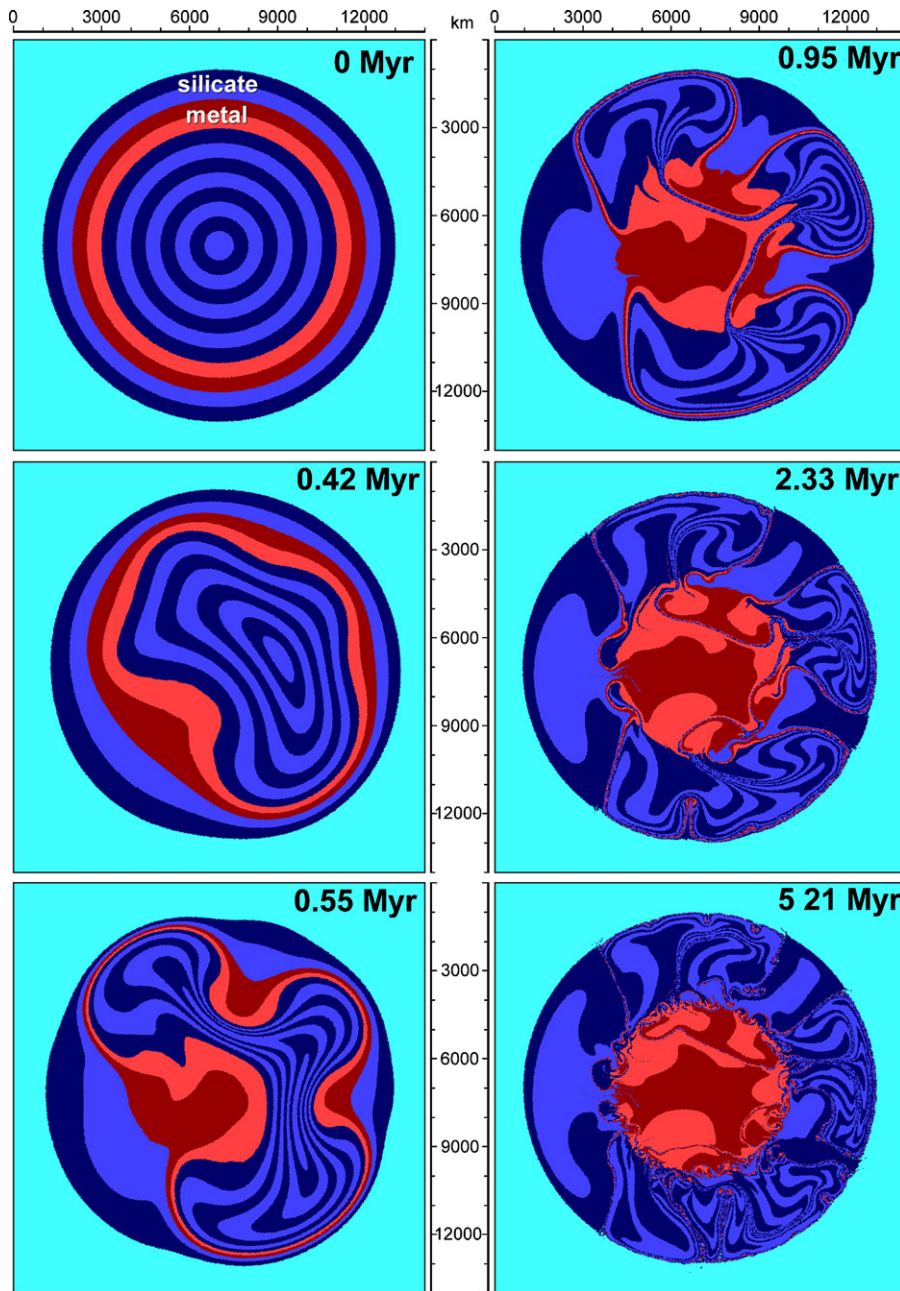


Fig. 11. Results of 2D numerical test for “soft shell tectonics” (Gerya et al., 2007): destabilisation of global high density (red) layer (Stevenson, 1981) under self-gravitation (cf. Fig. 10) for the case of dominating viscous deformation of planetary materials. Constant viscosity ($\eta = 10^{22}$ Pa s) of both silicate (dark to medium blue, $\rho = 4000$ kg/m³) and metal (red, $\rho = 10,060$ kg/m³). Low viscosity contrast (10^1) at the planetary surface at the contact with weak low density medium (light blue, $\rho = 1$ kg/m³) is used in this experiment. Grid resolution of the model is 141×141 nodes, 490,000 randomly distributed markers. (For interpretation of the references to colour in this figure legend, the reader is referred to the web version of the article.)

We also performed numerical tests for destabilisation of global metal layer formed around silicate-rich (primordial) core during planetary accretion (Stevenson, 1981) for the cases of dominating (i) viscous (Fig. 11)

and (ii) plastic (Fig. 12) deformation of planetary materials. As follows from our recent experiments (Gerya et al., 2007) this destabilization breaks the spherical symmetry of the planet and, therefore, cannot be

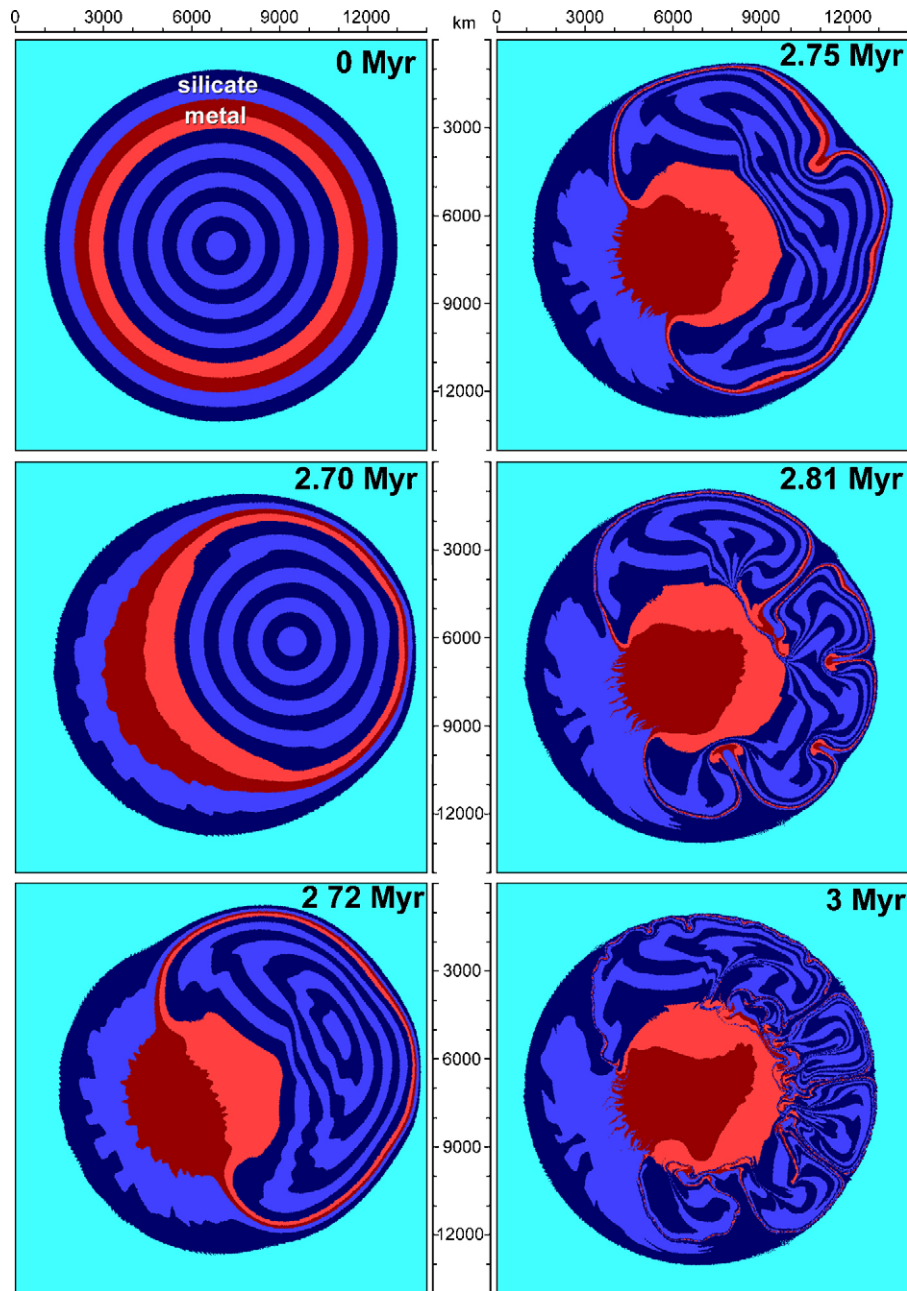


Fig. 12. Results of 2D numerical test for “hard shell tectonics” (Gerya et al., 2007): destabilisation of global high density (red) layer (Stevenson, 1981) under self-gravitation (cf. Fig. 10) for the case of dominating plastic deformation of planetary materials. Temperature dependent viscosity (dry olivine flow law, (Ranalli, 1995)) and lowered plastic strength are applied for both silicate ($\sin(\varphi)=0.1$, $C=10$ MPa) and metal ($\sin(\varphi)=0$, $C=10$ MPa). Thermal feedback from shear heating (Fig. 13) and high viscosity contrast (up to 10^5) at the planetary surface is used in this experiment. Other parameters are the same as for Fig. 11. (For interpretation of the references to colour in this figure legend, the reader is referred to the web version of the article.)

addressed properly in existing 1D models (e.g. Senshu et al., 2002) of planetary accretion. Metal layer destabilisation causes rapid planetary scale reshaping that we call “shell tectonics” (Gerya et al., 2007) as the

units involved in rearrangements are planetary shells. The gravitational redistribution process lasts within few Myr, which depends on the effective rheology, and is completely dominated in this period by shear

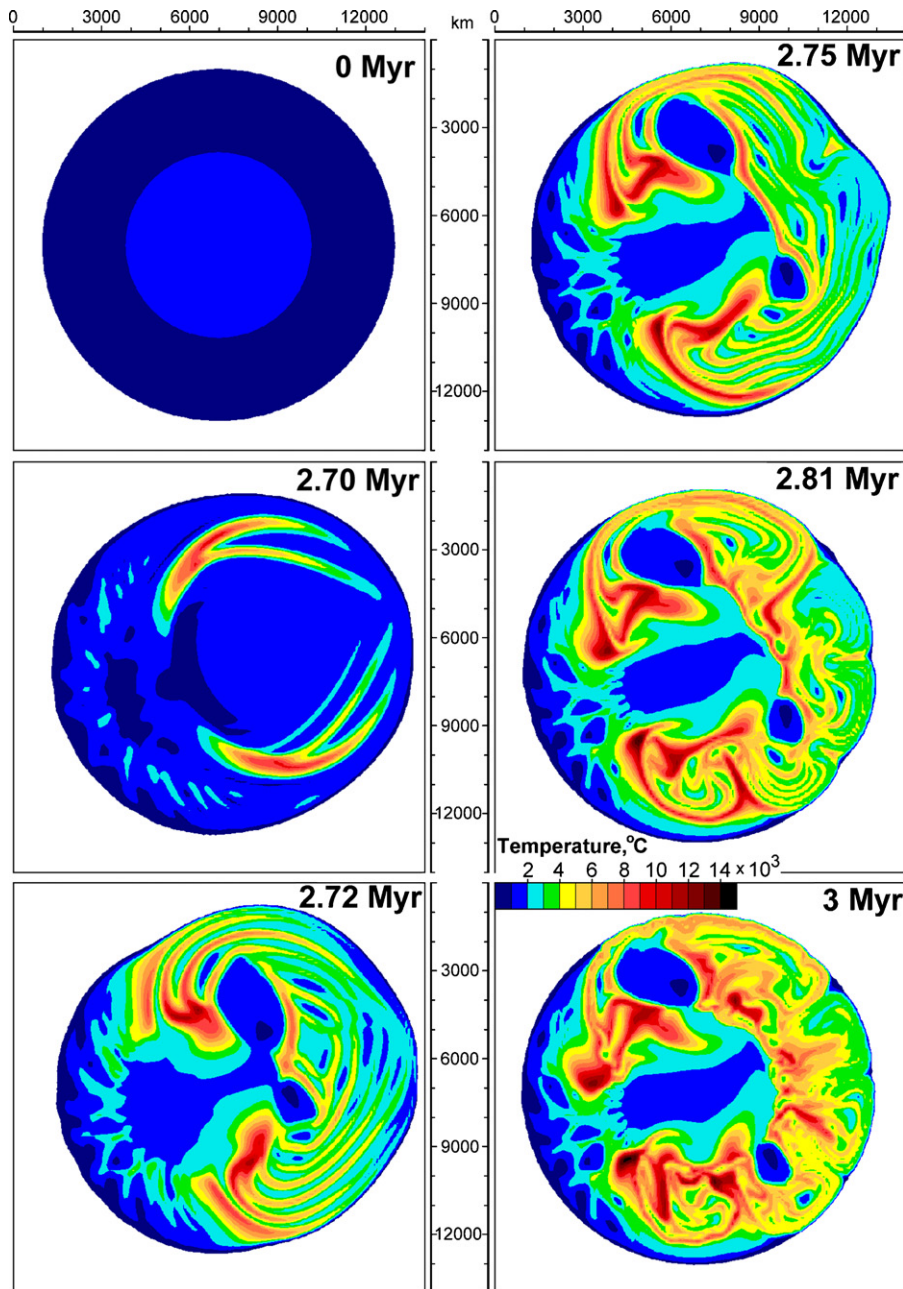


Fig. 13. Development of the temperature field due to shear heating along spontaneously forming localised deformation zones in case of numerical experiment for “hard shell tectonics” (Fig. 12).

heating (Fig. 13) and thermal advection. Internal gravitational redistribution processes result in planetary shape-changing revealing significant transient aspherical deviations from the original perfectly spherical geometry (Fig. 11, 0.55 Myr; Fig. 12, 2.72 Myr). During this stage the central silicate-rich core can become exposed at the planetary surface making possible its reworking during ongoing accretion processes. Most of

the enormous amount of heat is produced during this very short time span associated with the metallic core-formation and is then chaotically distributed throughout both the core and the mantle (Fig. 13, 3 Myr). Gravitational energy dissipation along the localized deformation zones (Fig. 13, 2.70–2.75 Myr) dramatically increases the rates of rearrangement and can potentially result in thermal runaway (Gruntfest, 1963) processes inside

the planet and sudden central silicate-rich primordial core fragmentation (Fig. 12, 2.70–2.81 Myr) (Stevenson, 1981). The magnitude of thermal perturbations can reach several thousand degrees, which cataclysmically raises the effective Rayleigh number for the planetary mantle to a very large number and possibly results in the formation of a magma ocean with the molten mantle rocks rising from the deep planetary interior. In future work, such instabilities should be considered in the context of ongoing planetary accretion first in 2D and then in 3D rather than starting from the equilibrium state of a 1D accretion model (e.g. Ida and Lin, 2004).

4. Discussion and future perspectives

In this paper we discuss further developments of our mixed Lagrangian-Eulerian numerical scheme based on conservative finite-differences and marker-in-cell techniques. We should really mention that the marker-in-cell technique is now broadly used in geodynamical modelling (cf. review Zhong et al., 2007) been combined with other numerical approaches such as

- finite volume method for pressure-velocity formulation (e.g. Tackley, 2000);
- finite-difference method for stream function formulation (e.g. Weinberg and Schmeling, 1992);
- finite-element method for pressure-velocity formulation (e.g., Moresi et al., 2003).

Important difference of our method compared to above marker-in-cell implementations is the use of markers for transport of *all* physical properties including the temperature advection and elastic stress rotation.

Using our previous code based on purely viscous rheologies (I2VIS) (Gerya and Yuen, 2003), we have since then pushed to the edge of present computational limits by breaking the *one billion* tracers mark and even exceed *ten billion* (Rudolph et al., 2004; Gorczyk et al., 2007). This very dense aggregate of tracers can be translated into an unprecedented resolution of a few meters in the regional problem of subduction dynamics. With a medium resolution of up to few tens of million tracers, we have also solved a number of important geodynamical problems, such as slab detachment (Gerya et al., 2004a,b), plumes in a mantle wedge (Gerya et al.,

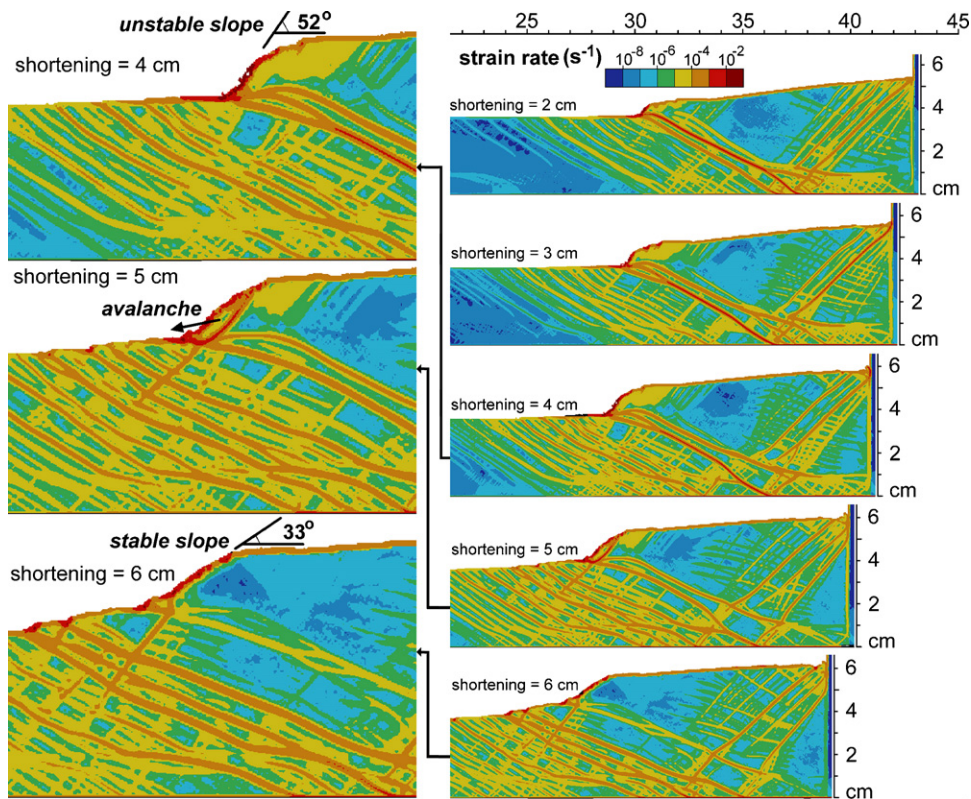


Fig. 14. Development of small-scale avalanche due to the spontaneous slope destabilization in high-resolution (grid resolution is $0.5 \text{ mm} \times 0.5 \text{ mm}$, 910×165 nodes, 1,500,000 markers) numerical sandbox shortening experiment (Fig. 5).

2006a; Górczyk et al., 2006) and the role of shear heating in orogenic metamorphism (Burg and Gerya, 2005). We have also developed coupled petrological–thermo-mechanical numerical modelling approach that takes into account dynamical rheological, thermal and density effects of phase transformations (including melting) based on the Gibbs free energy minimization (Gerya et al., 2004a,b, 2006a; Vasilyev et al., 2004). We have recently applied (Gerya et al., 2006a; Górczyk et al., 2006) this approach for numerical modelling of the seismic structure of thermal–chemical plumes beneath volcanic arcs.

Following the same “all-in-one” methodology (i.e. programming *all* various physical features *in one* numerical code) now we have developed a new version of this finite-difference, tracer code, coined I2ELVIS, which can handle visco-elasto-plastic rheology together with self-gravitation in a spherical body. We will emphasize the various new features, which were not present in the previous version of I2VIS. We include the following new capabilities:

- (1.) The code can handle complex non-linear rheology with time-derivatives of various order, such as

Maxwell visco-elastic and visco-elasto-plastic. The rheological constitutive equations are integrated in time by an explicit scheme. Tracers are used to delineate the spatial boundaries separating the various flow regimes at each time step.

- (2.) The conservation of mass equation is coupled to both the momentum and energy equations. Time-dependence is present in all three conservation equations, allowing thermo-mechanical–chemical and mass coupling at each time step. Multiple timescales associated with each equation are then linked together in this non-linear framework.
- (3.) Self-gravity is taken into account by solving the Poisson equation for the gravitational potential associated with the mass (density) distribution portrayed by the tracers at each time step. The gravitational vector whose direction depends on the mass distribution then governs the shape of the body embedded within a Cartesian coordinate system.

All three features hold within the framework of a 2D Cartesian geometry. As far as we know, there exists at present no single code, which can satisfy all of these three demands.

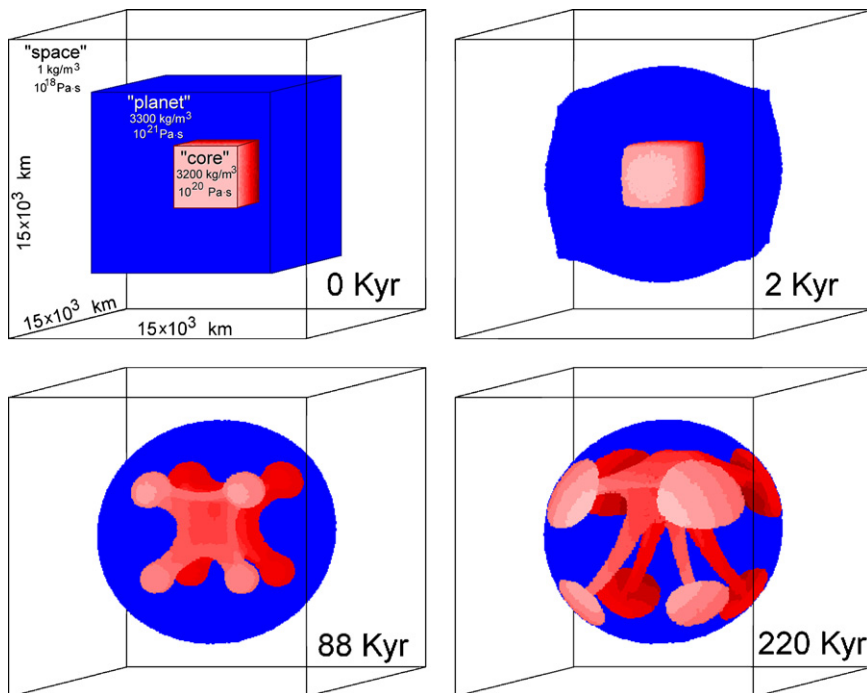


Fig. 15. Results of 3D numerical test with the code I3ELVIS using Cartesian grid, prescribed spherical gravity field and multigrid solver for continuity and momentum equations. Spherical planetary body (blue) is spontaneously formed from initial unstable cubic geometry. Large internal deformation of this body related to the rising of the buoyant core (red) does not destabilise numerical solution and planetary surface remains stable. Grid resolution of the model is $53 \times 53 \times 53$ nodes, 9,000,000 randomly distributed markers. (For interpretation of the references to colour in this figure legend, the reader is referred to the web version of the article.)

Here we address briefly the issue concerning the machine architecture and the non-linear-coupling in our “all-in-one” approach. The implementation of our system of non-linear equations, which couple all of the governing PDEs, would be facilitated by a shared-memory machine with a large RAM using Open-MP (Gorczyk et al., 2007), rather than by a distributed system using MPI, which could be less efficient in achieving the same error bounds because of problems in communications among the different domains during the iterative process.

In Fig. 14 we emphasize the importance of the sensitivity of the local convergence method used in satisfying the plastic-yield criterion (Eq. (2)) at each Lagrangian point and at every time step. If these strenuous criteria are not satisfied, it is then impossible to generate these clean-cut shear bands resulting from small-scale avalanches being zoomed in Fig. 14. One would obtain instead rather

diffused broad deformation zones. Further progress can be achieved in this direction by combining large amount (up to tens of billions, Gorczyk et al., 2007) of markers with computational grid refinement algorithms (e.g., Albers, 2000; Bergdorf and Koumoutsakos, 2006) and compressed wavelet-based representation and storage (Vasilyev et al., 2004) of continuous–discontinuous scalar, vector and tensor fields defined in Eulerian nodal points (Fig. 1) and on Lagrangian markers.

What is next in store for us? To make the code parallel using a combination of MPI and Open-MP and also the implementation of multigrid for the solving the momentum and continuity equations in 3D will be foremost on our agenda. We have already developed the 3D multigrid-based version of a “spherical-Cartesian” model and the preliminary results are displayed in Fig. 15. We can observe that the timescale for the evolution to a spherical equilibrium is defined by effective

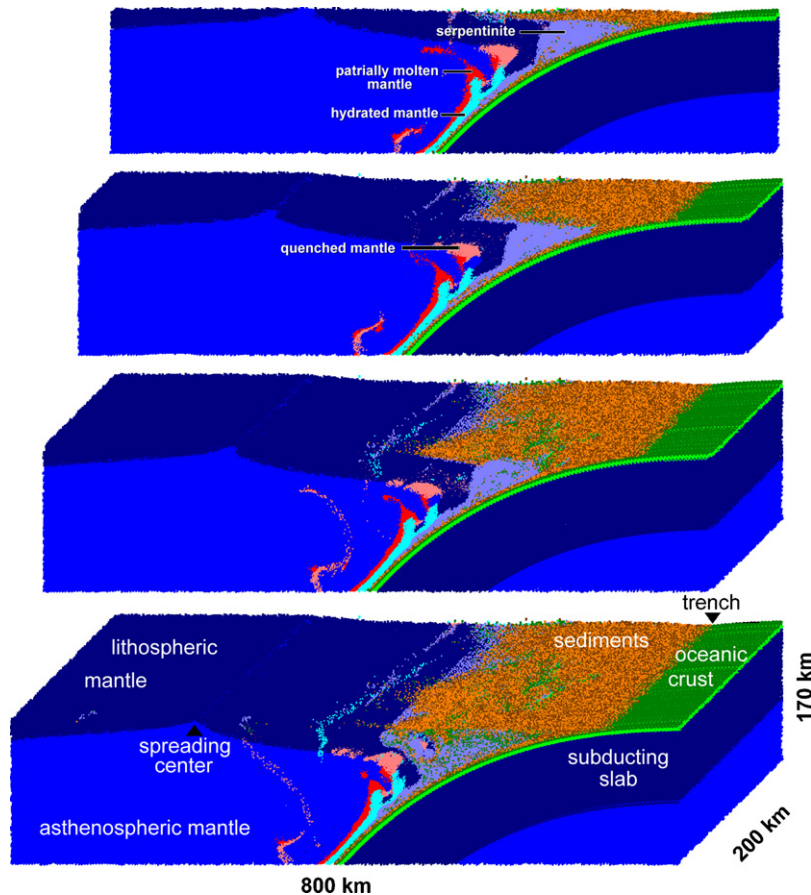


Fig. 16. Results of 3D numerical test with the code I3ELVIS using Cartesian grid, prescribed vertical gravity field and multigrid solver for continuity and momentum equations. Three-dimensional petrological–thermo-mechanical (Gerya et al., 2006a) model of intra-oceanic subduction accounts for free surface development, spontaneous slab bending and back-arc spreading as well as mantle wedge hydration and melting (e.g. Gerya et al., 2006a; Gorczyk et al., 2006). Four different vertical slices throughout the model are shown. Grid resolution of the model is $261 \times 101 \times 101$ finite-difference nodes, 10,000,000 randomly distributed markers.

viscosity of the body and is around 100,000 years when the viscosity is on the order of 10^{21} Pa s. This new code is also applicable for Cartesian geometry with prescribed vertical gravity field allowing to model regional tectonic processes in 3D. Fig. 16 shows example of the 3D

petrological–thermo-mechanical (Gerya et al., 2006a) model of intra-oceanic subduction which accounts for the dynamics of free surface, spontaneous slab bending, back-arc spreading and thermal–chemical plumes propagation (e.g. Gerya et al., 2006a; Gorczyk et al., 2006).

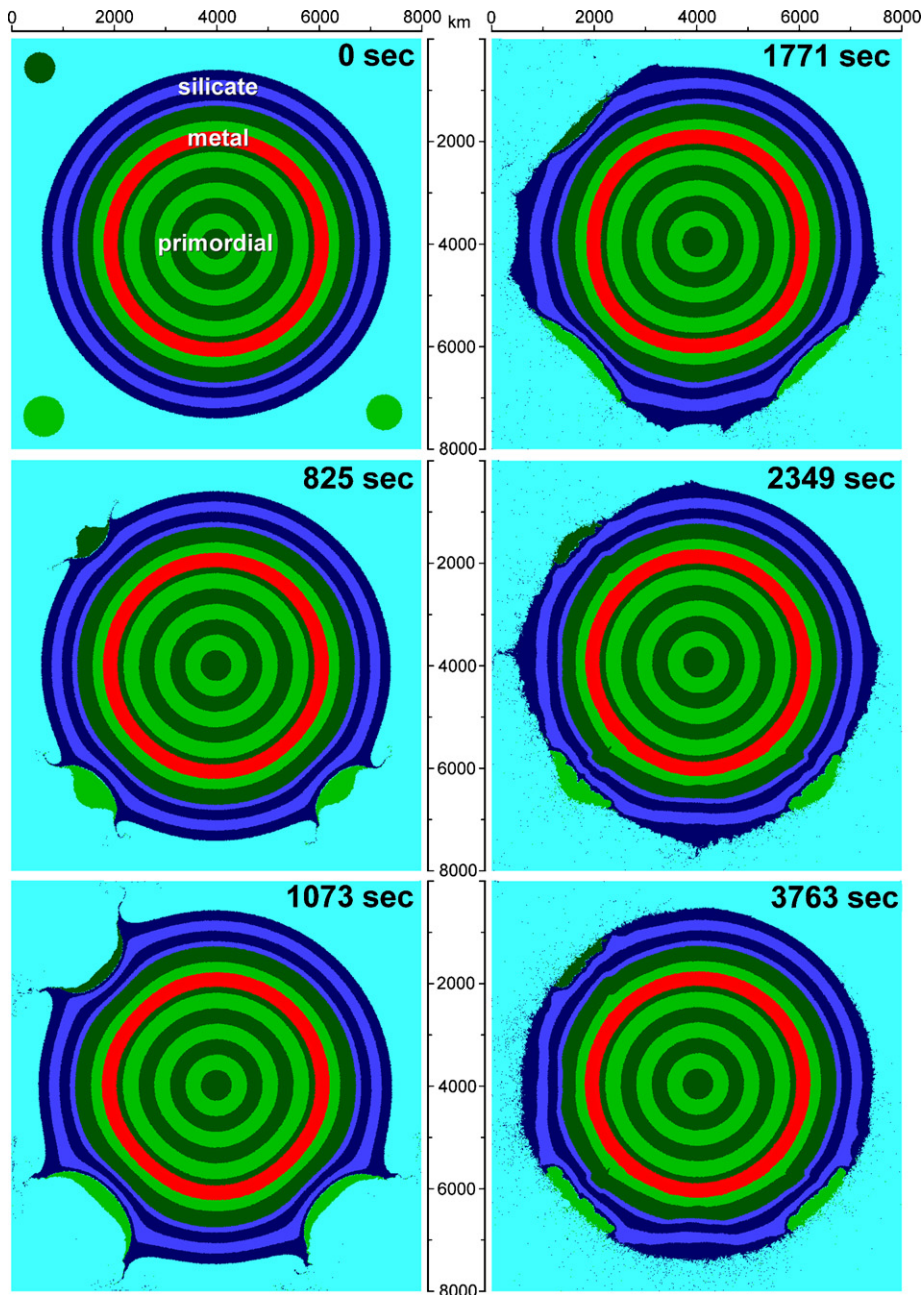


Fig. 17. Results of preliminary numerical experiments on a planetary accretion process associated with large meteorite (planetesimal) impacts. The experiment is performed for self-gravitating Mars-size body with the use of new developing version of visco-elasto-plastic code I2ELVIS which also treats inertial terms in momentum equations. Accretion process lasts for around one hour and associates with large amount of ejects, large elastic waves propagating along the planetary surface and elasto-plastic deformation of the interior. Grid resolution of the model is 161×161 nodes, 640,000 randomly distributed markers.

Using the tracers, we can also solve the momentum equation with the inertial terms taken into account. This operation is accomplished by an averaging process to calculate the effective momentum produced by the swarm of tracers within a given control volume. The temporal changes in the linear momentum give rise to the local inertial force within this volume, according to Newton's second law. We show in Fig. 17 the preliminary results for a swarm of large meteorites (planetesimals) hitting a planetary body with a visco-elasto-plastic rheology. We can see that penetration process is followed by the excavation and subsequent rebound dynamics in the crater created by the impact. Of course, in these extreme circumstances we must employ realistic equation of state for rocks (Kieffer, 1975; Cohen, 2000). This type of demand would create a tighter bond between modellers and computational mineral physicists.

Our new tack of including the inertial terms would also be very helpful in studying short-time instabilities which may produce slow earthquakes (Regenauer-Lieb and Yuen, 2006). We plan also to look into the problem post-seismic deformation and stress-transfer in triggering earthquakes (Stein, 1999; Chery et al., 2001), which are of direct societal relevance and concerns.

Acknowledgements

This work was supported by ETH Research Grants TH-12/04-1, TH-12/05-3, SNF Research Grant 200021-113672/1 and NSF grants from the ITR and CSEDI programs. We thank fruitful discussions with Paul J. Tackley, Boris J.P. Kaus, James A.D. Connolly, Klaus Regenauer-Lieb, Yuri Y. Podladchikov and Oleg V. Vasilyev. We greatly appreciate the very constructive and thorough reviews and suggestions offered by Louis Moresi and Charley Kameyama.

References

- Albers, M., 2000. A local mesh refinement multigrid method for 3D convection problems with strongly variable viscosity. *J. Comput. Phys.* 160, 126–150.
- Bergdorf, M., Koumoutsakos, P., 2006. A Lagrangian particle–wavelet method. *Multiscale Model. Simul.* 5 (3), 980–995.
- Brace, W.F., Kohlstedt, D.T., 1980. Limits on lithospheric stress imposed by laboratory experiments. *J. Geophys. Res.* 85, 6248–6252.
- Brackbill, J.U., 1991. FLIP MHD: a particle-in-cell method for magnetohydrodynamics. *J. Comput. Phys.* 96, 163–192.
- Buiter, S.J.H., Babeyko, A.Yu., Ellis, S., Gerya, T.V., Kaus, B.J.P., Kellner, A., Schreurs, G., Yamada, Y., 2006. The numerical sandbox: comparison of model results for a shortening and an extension experiment. In: Buiter, S.J.H., Schreurs, G. (Eds.), *Analogue and Numerical Modelling of Crustal-Scale Processes*, 253. Geological Society, Special Publications, London, pp. 29–64.
- Burg, J.-P., Gerya, T.V., 2005. Viscous heating and thermal doming in orogenic metamorphism: numerical modeling and geological implications. *J. Metamorph. Geol.* 23, 75–95.
- Chery, J., Carretier, S., Ritz, J.F., 2001. Postseismic stress transfer explains time-clustering of large earthquakes in Mongolia. *Earth Planet. Sci. Lett.* 194, 277–289.
- Cohen, R., 2000. *Physics Meets Mineralogy*. Cambridge University Press.
- Gerya, T.V., Burg, J.-P., 2007. Intrusion of ultramafic magmatic bodies into the continental crust: numerical simulation. *Phys. Earth Planet. Interiors* 160, 124–142.
- Gerya, T.V., Yuen, D.A., 2003. Characteristics-based marker-in-cell method with conservative finite-differences schemes for modeling geological flows with strongly variable transport properties. *Phys. Earth Planet. Interiors* 140, 295–320.
- Gerya, T.V., Perchuk, L.L., Maresch, W.V., Willner, A.P., 2004a. Inherent gravitational instability of hot continental crust: implication for doming and diapirism in granulite facies terrains. In: Whitney, D., Teyssier, C., Siddoway, C.S. (Eds.), *Gneiss Domes in Orogeny*, The Geological Society of America Special Paper 380, The Geological Society of America, Boulder, Colorado, pp. 97–115.
- Gerya, T.V., Yuen, D.A., Maresch, W.V., 2004b. Thermomechanical modeling of slab detachment. *Earth Planet. Sci. Lett.* 226, 101–116.
- Gerya, T.V., Connolly, J.A.D., Yuen, D.A., Gorczyk, W., Capel, A.M., 2006a. Seismic implications of mantle wedge plumes. *Phys. Earth Planet. Interiors* 156, 59–74.
- Gerya, T.V., Connolly, J.A.D., Yuen, D.A., 2006b. Fluids and melts in subduction zones: insight from numerical modelling. In: *EGU 2006, Geophysical Research Abstracts*, vol. 8, p. 07259.
- Gerya, T.V., Tackley, P.J., Yuen, D.A., 2007. Shear heating, shell tectonics and core formation. In: *EGU 2007, Geophysical Research Abstracts* 9.
- Gorczyk, W., Gerya, T.V., Connolly, J.A.D., Yuen, D.A., Rudolph, M., 2006. Large-scale rigid-body rotation in the mantle wedge and its implications for seismic tomography. *Geochem. Geophys. Geosyst.* 7, Q05018, doi:10.1029/2005GC001075.
- Gorczyk, W., Gerya, T.V., Connolly, J.A.D., Yuen, D.A., 2007. Growth and mixing dynamics of mantle wedge plumes. *Geology* 35, 587–590.
- Gruntfest, I.J., 1963. Thermal feedback in liquid fluid: plane shear at constant stress. *Trans. Soc. Rheol.* 8, 195–207.
- Hall, C.E., Gurnis, M., Sdrolias, M., Lavier, L.L., Muller, R.D., 2003. Catastrophic initiation of subduction following forced convergence across fractures zones. *Earth Planet. Sci. Lett.* 212, 15–30.
- Hill, R., 1950. *The Mathematical Theory of Plasticity*. Oxford University Press, Oxford, 366 pp.
- Ida, S., Lin, D.N.C., 2004. Toward a deterministic model of planetary formation. II. *Astrophys. J.* 616, 567–572.
- Joseph, D.D., 1990. *Fluid Dynamics of Viscoelastic Fluids*. Springer-Verlag, New York, 755 pp.
- Kameyama, M., Yuen, D.A., Karato, S., 1999. Thermal-mechanical effects of low-temperature plasticity (the Peierls mechanism) on the deformation of a viscoelastic shear zone. *EPSL* 168, 159–172.
- Kieffer, S., 1975. From regolith to rock by shock. *J. Earth Moon Planets* 13, 301–320.
- Moresi, L., Dufour, F., Mühlhaus, H.-B., 2003. A Lagrangian integration point finite element method for large deformation modeling of viscoelastic geomaterials. *J. Comput. Phys.* 184, 476–497.
- Mühlhaus, H.B., Regenauer-Lieb, K., 2005. Towards a self-consistent plate mantle model that includes elasticity: simple benchmarks and application to basic modes of convection. *Geophys. J. Int.* 163, 788–800.

- Patankar, S.V., 1980. *Numerical Heat Transfer and Fluid Flow*. McGraw-Hill, New York.
- Poliakov, A.N.B., Herrmann, H.J., 1994. Self-organized criticality of plastic shear bands in rocks. *Geophys. Res. Lett.* 21, 2143–2146.
- Ranalli, G., 1995. *Rheology of the Earth*. Chapman & Hall, London, 413 pp.
- Ranero, C.R., Morgan, J.P., McIntosh, K., Reichert, C., 2003. Bending-related faulting and mantle serpentinization at the Middle America trench. *Nature* 425, 367–373.
- Ranero, C.R., Villasenor, A., Morgan, J.P., Weinrebe, W., 2005. Relationship between bend-faulting at trenches and intermediate-depth seismicity. *Geochem. Geophys. Geosyst.* 6 (Art. no. Q12002).
- Regenauer-Lieb, K., Yuen, D.A., 2004. Positive feedback of interacting ductile faults from coupling of equation of state, rheology and thermo-mechanics. *Phys. Earth Planet. Interiors* 142, 113–135.
- Regenauer-Lieb, K., Yuen, D.A., 2006. Quartz rheology and short-time-scale crustal instabilities. *Pure Appl. Geophys.* 163, 1915–1932.
- Rudolph, M.L., Gerya, T.V., Yuen, D.A., DeRosier, S., 2004. Visualization of multiscale dynamics of hydrous cold plumes at subduction zones. *Visual Geosci.* 17, 59, doi:10.1007/s10069-004-0017-2.
- Schmalholz, S.M., Podladchikov, Y.Y., Schmid, D.W., 2001. A spectral/finite difference method for simulating large deformations of heterogeneous, viscoelastic materials. *Geophys. J. Int.* 145, 199–208.
- Senshu, H., Kuramoto, K., Matsui, T., 2002. Thermal evolution of a growing Mars. *J. Geophys. Res.* 107, 5118, doi:10.1029/2001je001819.
- Stein, R., 1999. The role of stress transfer in earthquake occurrence. *Nature* 402, 605–609.
- Stevenson, D.J., 1981. Models of the Earth's core. *Science* 214, 611–619.
- Tackley, P.J., 2000. Self-consistent generation of tectonic plates in time-dependent, three-dimensional mantle convection simulations. Part 1. Pseudo-plastic yielding. *Geochem. Geophys. Geosyst.* 1 (Paper no. 2000GC000036).
- Ten, A.A., Yuen, D.A., Podladchikov, Yu.Yu., 1999. Visualization and analysis of mixing dynamical properties in convecting systems with different rheologies. *Electron. Geosci.*, 4.
- Turcotte, D.L., Schubert, G., 2002. *Geodynamics*. Cambridge University Press, Cambridge, 456 pp.
- Vasilyev, O.V., Gerya, T.V., Yuen, D.A., 2004. The application of multi-dimensional wavelets to unveiling multi-phase diagrams and in situ physical properties of rocks. *Earth Planet. Sci. Lett.* 223, 49–64.
- Vermeer, P.A., 1990. The orientation of shear bands in biaxial tests. *Geotechnique* 40, 223–236.
- Weinberg, R.B., Schmeling, H., 1992. Polydiapirs: multiwavelength gravity structures. *J. Struct. Geol.* 14, 425–436.
- Zhong, S., Yuen, D.A., Moresi, L.N., 2007. Numerical methods for mantle convection. In: Bercovici, D. (Ed.), *Mantle Dynamics*, Treatise on Geophysics, vol. 7, Elsevier, in press.